

**Hydrodynamic density-functional theory for the moving
contact-line problem reveals fluid structure and emergence of a
spatially distinct pattern.**

Andreas Nold

*Theory of Neural Dynamics, Max Planck Institute for Brain Research,
60438 Frankfurt am Main, Germany*

Benjamin D. Goddard

*The School of Mathematics and Maxwell Institute for Mathematical Sciences,
The University of Edinburgh, Edinburgh, EH9 3FD, UK*

David N. Sibley

*Department of Mathematical Sciences,
Loughborough University, Loughborough, LE11 3TU, UK*

Serafim Kalliadasis*

*Department of Chemical Engineering,
Imperial College London, London, SW7 2AZ, UK*

(Dated: December 10, 2024)

Abstract

Understanding the nanoscale effects controlling the dynamics of a contact line – defined as the line formed at the junction of two fluid phases and a solid – has been a longstanding problem in fluid mechanics pushing experimental and numerical methods to their limits. A major challenge is the multiscale nature of the problem, whereby nanoscale phenomena manifest themselves at the macroscale. To probe the nanoscale, not easily accessible to other methods, we propose a reductionist model that employs elements from statistical mechanics, namely dynamic-density-functional theory (DDFT), in a Navier-Stokes-like equation – an approach we name hydrodynamic DDFT. The model is applied to an isothermal Lennard-Jones-fluid with no slip on a flat solid substrate. Our computations reveal fluid stratification with an oscillatory density structure close to the wall and the emergence of two distinct regions as the temperature increases: a region of compression on the vapor side of the liquid-vapour interface and an effective slip region of large shear on the liquid side. The compressive region spreads along the fluid interface at a lengthscale that increases faster than the width of the fluid interface with temperature, while the width of the slip region is bound by the oscillatory fluid density structure and is constrained to a few particle diameters from the wall. Both compressive and shear effects may offset contact line friction, while compression in particular has a disproportionately high effect on the speed of advancing contact lines at low temperatures.

I. INTRODUCTION

Wetting or dewetting – the fluid mechanical process of a liquid phase expanding or shrinking its contact area with a solid substrate – is ubiquitous in nature and technology [1]. Central to any description of wetting or dewetting is the presence of a moving contact line, the line formed by the intersection of a fluid-fluid interface with a solid substrate (see Fig. 1). Classical fluid mechanics predicts that the force at the contact line is infinite, an unphysical result called the “contact line singularity” [2, 3]. It is often concluded that nanoscale effects, neglected in the standard continuous models, resolve the singularity. However, as of yet it is unclear what the precise role of these effects is and how they manifest to influence macroscale behavior.

* s.kalliadasis@imperial.ac.uk

Experimental, numerical and theoretical approaches have provided clues towards possible solutions, but each approach faces its own unique challenges. Experimental measurements cannot capture single particle dynamics [4–6]. Numerical particle-based, i.e. molecular dynamics (MD) simulations have allowed for valuable insights into nanodroplet dynamics. They are, however, limited due to low signal-to-noise ratios, also present in experimental techniques, prohibitive computational costs [7], theoretical assumptions imposed by unconstrained approximations such as the thermostat choice as well as boundary conditions [8], and high number of parameters and degrees of freedom [9]. For instance, a global thermostat, such as Nosé-Hoover, for problems in the presence of shear can lead to thermal energy production close to solid boundaries higher than the one in the bulk, potentially causing a non-uniform temperature distribution in a fluid, especially at low temperatures. On the theoretical front, one of the earliest models, molecular kinetic theory (MKT) [10], views wetting as an activated chemical adsorption process. Its relation of contact line friction to the off-equilibrium driving force is obtained as a constitutive law following thermodynamic arguments [11], and was later used as a nanoscale boundary condition for the viscocapillary regime [11, 12]. [This region, where viscous effects balance surface tension, is discussed in detail in [13] where the asymptotics of the hydrodynamic moving contact line problem were carefully revisited highlighting some misconceptions with certain technical details in the asymptotic analysis of previous works, e.g. by Hocking and Cox [14].] Other approaches introduce time- and density-dependent surface tensions [15], or generalized Navier boundary conditions which combine slip, viscous stress, and uncompensated Young stress [16]. However, by design these models include at least one phenomenological parameter and fall short of identifying the precise nanoscale effects that determine the fluid structure and compete to resolve the contact line singularity, and, not surprisingly, drawing significant debate about model choices and validity [17–19].

To circumvent the experimental and numerical-theoretical limitations, we follow a theoretical framework based on the statistical mechanics of classical fluids, namely density-functional theory (DFT) [20], which naturally includes particle-level information. As highlighted by Lutsko [21], the advantage of DFT over other theories, e.g. diffuse interfaces, is that it is, in principle, *ab initio* offering a quantitatively accurate representation of molecular-scale correlations and structure; a fundamental foundational theory and from which other theories can be viewed as approximations. It has been successfully applied to highly non-

uniform systems from wetting, thin films and drops [22–25], crystal structures– crystallization [21, 26] and solidification [27], to complex fluids such as polymers [28, 29] and lipid bilayers [30], and molecular self-assembly [31]. DFT has been extended to dynamics, the so-called dynamic DFT (DDFT), which describes not only equilibrium but also the dynamic behavior out of equilibrium, and has been validated in a wide variety of situations, showing excellent agreement with stochastic/Langevin simulations [32–35]. Here DDFT will be applied to a problem that simulations cannot easily tackle. In this direction we couple DDFT with a hydrodynamic model, a generalisation which we refer to as hydrodynamic DDFT (HDDFT). It results in a reductionist continuum model that depends on the fluid viscosity and three truly fundamental parameters of the system: fluid temperature, fluid-fluid, and wall-fluid interactions (these interactions in turn depend on the interatomic potential). It retains information from the particle scale while also capturing the viscocapillary region. It therefore enables scrutiny of the molecular organisation of the moving contact line in the immediate vicinity of the contact point. In particular, we can probe the nanoscale behavior as the temperature varies, inaccessible with other experimental and numerical approaches, such as MD, and so far remains largely unstudied.

To check consistency with meso- and macroscopic predictions and experimental results, we show that HDDFT recovers a linear relationship between contact line velocity and force, analogous to molecular kinetic theory (MKT), with the contact line friction as a parameter [10]. HDDFT also provides predictions for the contact line friction as a function of temperature and wall attraction for hitherto unprobed values.

Zooming into the nanoscale region of the contact line, we observe fluid stratification with an oscillatory density structure close to the wall and the emergence of two distinct regions: a shear region which extends along the wall – and a compression region on the vapor side of the liquid-vapor interface. The results presented here raise the prospect that the correct incorporation of fluid layering and the competition of compressive versus shear effects at the contact line are the missing pieces to understanding the nanoscale effects governing contact line motion.

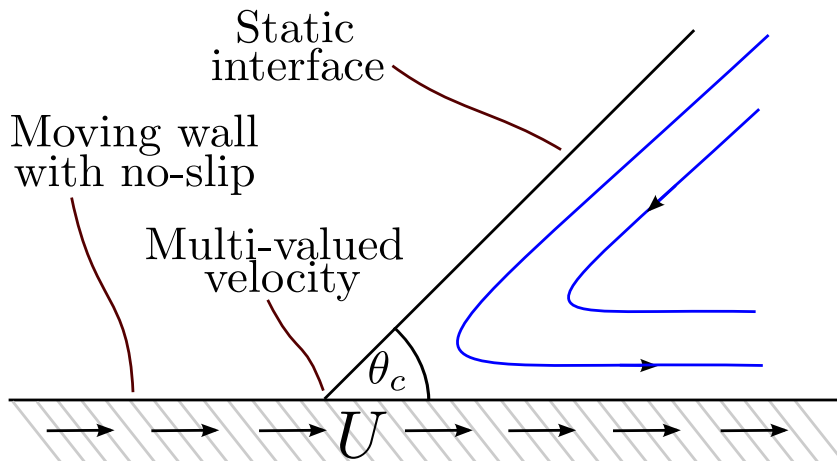


FIG. 1. Sketch of a stationary interface in contact with a wall moving with velocity U with no slip. θ_c denotes the microscopic contact angle, i.e. the contact angle right at the contact point. Classical hydrodynamic theory results in a multivaluedness of the velocity, with the consequence that the hydrodynamic problem has no solution, and associated with this, the shear stress and pressure are singular at the contact point with a $1/r$ singularity, with r the distance from the contact point (hence a non-integrable shear-stress/pressure singularity) [2].

II. HDDFT

For a simple fluid at the nanoscale, we assume that the stress tensor is isotropic and that it is a function of the local density of the fluid. We also assume that particle-particle interactions act non-locally as a body force on other parts of the fluid. This is equivalent to replacing the pressure-term in the momentum equation of the Navier-Stokes equations by $-n\nabla\mu$, where the chemical potential μ is given by

$$\mu = \frac{\delta\mathcal{F}}{\delta n} + V_{\text{ext}}, \quad (1)$$

where \mathcal{F} is the DFT free-energy functional, V_{ext} is the external potential and $n = \rho/m$ is the number density with m the fluid particle mass and ρ the density. In contrast to equilibrium DFT, μ is not a constant, but a function of space and time. This approach is in some sense similar to the one followed diffuse interface models, which employ a square-gradient expansion of the free energy of the system, and for which the term $-n\nabla\mu$ accounts for surface tension effects via the so-called Korteweg stress tensor [36, 37]. However, the local

expansion employed in diffuse-interface models has certain shortcomings as highlighted in our previous effort in Ref. [38]. It does not capture layering effects and can lead to multi-valued curves for the adsorption isotherm (effectively the thickness of a film adsorbed on a flat substrate as a function of the distance of the chemical potential from its saturation value), thus predicting phase transitions in regions where there are none. There is also another more subtle issue with diffuse-interface models. The models contain unknown and ad-hoc parameters, in particular the interface width, say ε , which is not known a priori. For sure, it has to be much larger than the molecular scale, the hard sphere diameter σ , $\varepsilon \gg \sigma$, as the diffuse-interface models do not have any molecular information and this separation of scales is necessary. At the same time, ε must be much smaller than a characteristic macroscale in the system, say l_{macro} , $\varepsilon \ll l_{\text{macro}}$, and in fact the ratio of the two is taken to be small to show that the usual hydrodynamic equations for the particular fluid flow setting at hand are recovered, e.g. [39].

Here, we go beyond the local expansion and employ the DFT free-energy functional, which is fully nonlocal. The interface width is no longer an issue as the density gradient across the interface can be computed directly (from which an effective interface width can be extracted, if so desired). The fluid itself is assumed to be a Lennard-Jones (LJ) one, the standard prototypical model of MD, with an intermolecular potential originating (at least in part) from quantum mechanics, and appropriate for an idealised system like liquid Argon (more involved models are often invoked in MD but the results obtained with LJ are qualitatively satisfactory). The solid is also taken as LJ and is modelled via an effective potential derived from fluid-solid interparticle interactions. This mean-field approximation makes the wall homogeneous and ideally-smooth with the same structure throughout, thus avoiding details about its atomistic structure; details on DFT, and on the fluid and solid models employed are given in Appendix A.

The HDDFT model consists of the continuity and the momentum equations,

$$\frac{\partial n}{\partial t} + \nabla \cdot (n\mathbf{u}) = 0, \quad (2a)$$

$$mn \left(\frac{\partial \mathbf{u}}{\partial t} + \mathbf{u} \cdot \nabla \mathbf{u} \right) = -n \nabla \left(\frac{\delta \mathcal{F}}{\delta n} \right) + \nabla \cdot \boldsymbol{\tau}, \quad (2b)$$

where $\boldsymbol{\tau} = \zeta (\nabla \cdot \mathbf{u}) + \eta ((\nabla \mathbf{u} + (\nabla \mathbf{u})^T) - \frac{2}{3}(\nabla \cdot \mathbf{u})\mathbf{I})$ is the stress tensor, \mathbf{u} is the fluid velocity and η and ζ represent the shear (or dynamic) and bulk (accounting for compressible effects) viscosities, respectively. For simplicity, η and ζ are assumed to depend linearly on

the local fluid density. Further details on the HDDFT model are given in Appendix B, while values of liquid and vapour viscosities for all computations throughout are given in Table I there. Let us stress here that the Newtonian law is not stipulated but can be derived as part of the HDDFT framework [33].

The model developed here assumes constant temperature throughout the fluid. As discussed in Appendix A, in the static case, the fluid layering in the vicinity of a substrate computed by DFT is consistent with Monte Carlo computations at the respective temperature. The dynamic situation, however, is different: MD simulations employ thermostats to which the nanoscale dynamics in highly inhomogeneous systems is sensitive [8]. The method proposed here fulfills the bulk limit away from the wall commonly used to validate nanoscale models [9]. But its cornerstone is the DFT free-energy functional which as pointed out in Appendix A is formulated in a constant temperature – constant chemical potential ensemble. As such the framework proposed here is by design isothermal. This means that local temperature changes due to viscous heat production are neglected. In principle, these can be included by developing extended DDFTs, which also couple to an energy equation, but the temperature changes must be slow (quasistatic). An additional equation would inevitably increase the dimensionality of the problem and therefore the computational cost, and would be against our reductionist approach to formulate the simplest possible model. In Appendix C we show that the total temperature increase is likely not to exceed more than a few percent over the timescale of interest.

In our computations, we will consider chemical-potential-driven contact line motion. This means that the contact angle is initially off equilibrium and then approaches its equilibrium state. The bulk phases and fluid interfaces are at equilibrium away from the contact line and motion is therefore driven by nonequilibrium effects in the vicinity of the contact line alone. The model does not require slip to resolve the contact line singularity. In fact no slip is applied at the wall, which avoids the introduction of a slip length as an empirical parameter, in agreement with the reductionist paradigm advocated in this work.

III. FLUID STRUCTURE IN THE VICINITY OF THE CONTACT LINE

The emphasis is on the fluid structure close to the contact line. At equilibrium, the DFT computations show a well-defined defined interface in the form of a wedge in contact with the

substrate and with a well-defined contact angle, as in our previous studies (which focused at equilibrium) [38, 40–43] (e.g. Fig. 8 in Ref. [38]). This wedge seems to persist for distances sufficiently far from the substrate, and it should eventually enter the macroscale, and should allow us to connect the micro- with the macroscale. As illustrated in Fig. 2, the DFT computations of the contact angle also follow closely Young’s equation, again in agreement with our previous studies [40, 41], revealing also an incredible fact about the equation: it is based on purely macroscopic arguments, yet it is valid all the way to the nanoscale. As expected, the contact angle decreases with increasing wall-fluid attraction ε_{wf} [38]. Strong wall-fluid attractions ε_{wf} induce packing of fluid particles and large oscillations of the density profile in the vicinity of the wall. The opposite effect is seen for large contact angles and low wall-fluid attractions, where the formation of a quasi-vapor film is observed [40, 41]. The connection with disjoining pressure and interfacial Hamiltonian approaches was discussed in Ref. [40] while in Ref. [43] another incredible fact was revealed: density profiles at a three-phase contact line may be described approximately by the density profile of a flat film provided by the distance measured along the normal to the interface. As was already alluded to in Ref. [38], to understand contact lines it is essential that one understands the case of flat film on a substrate first.

Figure 3 depicts velocity and density fields for an advancing contact line. The density oscillations and fluid structure observed at equilibrium persist in the dynamic state. Energy is dissipated through transport of matter across the fluid interface as well as shear. Classical thermodynamics quantifies the rate at which configurational and kinetic energy is transformed into thermal energy as the viscous energy dissipation $\dot{\varepsilon}_v$ [44]:

$$\dot{\varepsilon}_v = \underbrace{\zeta (\nabla \cdot \mathbf{u})^2}_{\text{compression}} + \eta \underbrace{\frac{1}{2} \left((\nabla \mathbf{u} + (\nabla \mathbf{u})^T) - \frac{2}{3} (\nabla \cdot \mathbf{u}) \mathbf{I} \right)^2}_{\text{shear}}, \quad (3)$$

where the square of the tensor is defined as the sum of its squared elements, including a third dimension with all pertinent quantities set to zero. Away from the contact line, the system moves in a purely convective manner. However, sufficiently close to the contact line mass transport across the liquid-vapor interface takes over, as seen by the compression of two streamlines across the interface. As a consequence, a caterpillar-rolling motion-like behavior is observed in the liquid phase, whilst the vapor phase is almost entirely compressed into, or decompressed from, the liquid phase for advancing and receding contact lines, respectively.

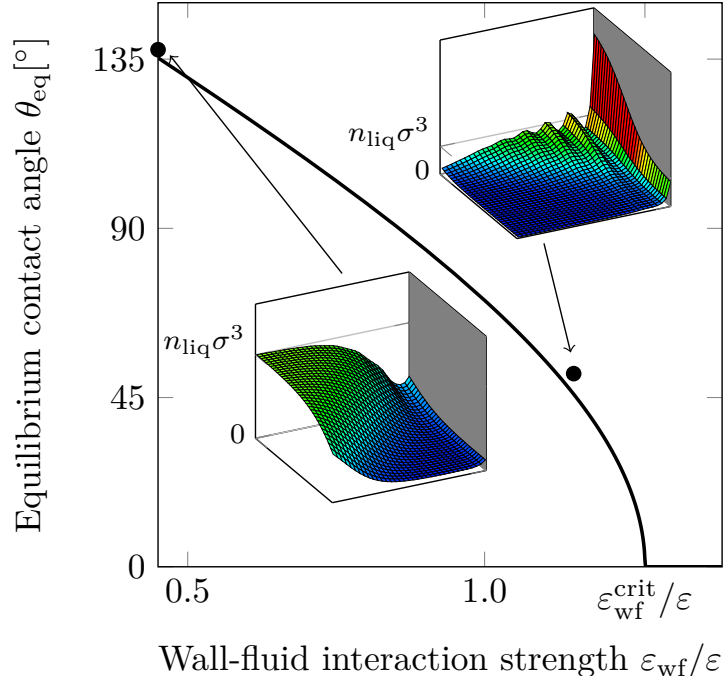


FIG. 2. Equilibrium contact angle θ_{eq} , computed via Young's equation based on the balance of wall-fluid and fluid-fluid surface tensions (solid line), and two-dimensional DFT computations (filled circles) as a function of normalized wall-fluid attraction $\varepsilon_{\text{wf}}/\varepsilon$ at the low temperature $k_B T = 0.75\varepsilon$. A comparison across the whole range of contact angles is given in Refs. [40, 41]. Insets show three-dimensional profiles of the equilibrium number density n on a $7\sigma \times 7\sigma$ area close to the wall, shown in grey (σ is the hard sphere diameter). $\varepsilon_{\text{wf}}^{\text{crit}}$ marks the transition to complete wetting.

In Appendix C we demonstrate that the total temperature increase due to viscous energy dissipation is likely not to exceed more than a few percent over the timescale of interest. This is due to the (realistically) low contact line velocities (Figs 10 and 11 of Appendix E) together with the particular spatial organisation of the dissipation regime.

IV. EMERGENT CONTACT LINE BEHAVIOR AT THE NANOSCALE

We will be looking at two temperatures: the low temperature $k_B T = 0.75\varepsilon$, and the high temperature $k_B T = 0.9\varepsilon$, relatively close to the critical point. Of course, DFT and consequently HDDFT, are mean-field approximations which ignore fluctuations and therefore are less reliable as criticality is approached, where fluctuations may play a dominant role. It is for this reason exactly that we avoid being too close to criticality. Our overarching

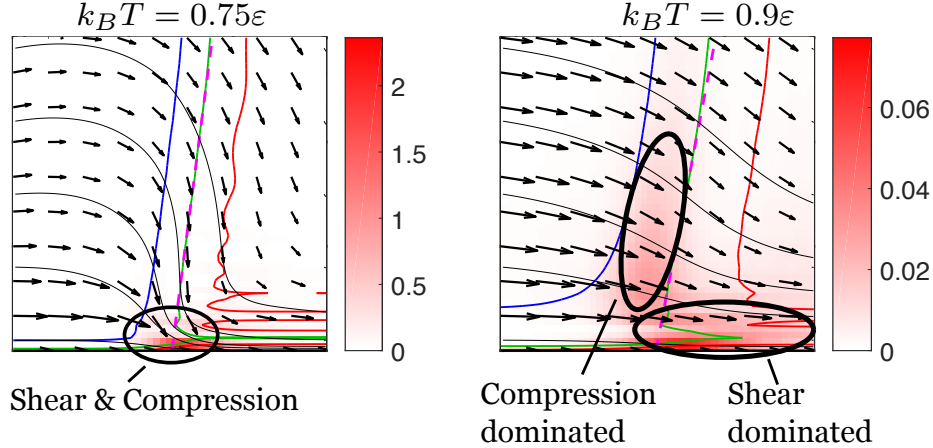


FIG. 3. HDDFT results for an advancing contact line at two temperatures relaxing from $\theta_{\text{in}} = 90^\circ$ to $\theta_{\text{eq}} = 60^\circ$ at $t = 250\tau$ on a $15\sigma \times 15\sigma$ square domain next to the wall. For low temperatures, shear and compression dominated regions are located in the immediate vicinity of the contact line. For high temperatures, the two regions separate in space, and extend along the fluid-wall and fluid-fluid interfaces, respectively. Isolines (colored solid lines), velocity field (arrows) and streamlines (black solid lines) are given relative to the motion of the contact line. The blue, green and red isolines for the density represent values $(n - n_{\text{vap}}) / (n_{\text{liq}} - n_{\text{vap}}) = \{0.05, 0.5, 0.95\}$, respectively. The dashed magenta line, obtained as a linear extrapolation of the green density isoline to the substrate, represents the dynamic fluid interface and acts as a guide for the eye. The blue and red isolines then are for the vapour and liquid phases, respectively, in the immediate vicinity of the interface. The colormap represents the entropy production $\dot{\epsilon}_v^* = \dot{\epsilon}_v \sigma^4 / (U_{\text{CL}}^2 \sqrt{\epsilon m})$, rescaled with the squared contact line velocity U_{CL} (see Eq. 3). A detailed overview of the dynamic evolution of receding and advancing contact lines at $k_B T = 0.75\epsilon$ and 0.9ϵ is given in Appendix E. Separate plots of shear and compression for the advancing and receding case are given in Fig. 4. Finally, how an effective liquid-vapour interface is calculated is given in the caption of Fig. 10 of Appendix E; the contact line position and contact angle have to be calculated with care – the contact angle, in particular, requires a careful measurement given all the terraces in the density profiles; details for the calculation of contact line position–contact angle are given in Appendix D.

objective here is to expose certain trends in contact line motion and uncover new patterns and insights as the temperature increases. By taking the temperature relatively close to the critical point a certain qualitative picture emerges, and our results show a clear pattern as

detailed below.

At temperature $k_B T = 0.75\epsilon$, most of the transfer of mechanical into thermal energy is concentrated in the immediate vicinity of the contact line. In contrast, raising the temperature to $k_B T = 0.9\epsilon$ removes the localization and viscous energy dissipation spreads along the wall and the vapor side of the fluid interface, as shown in Figs 3 and 4, with the dissipative region being separated into compressive and shear regions. Whilst some change of spatial distribution with temperature is expected, the difference exceeds the change suggested by the increase of the liquid-vapor interface width with temperature from 4.2σ for $k_B T = 0.75\epsilon$ to 7.3σ for $k_B T = 0.9\epsilon$. A separate study of compressive and shear regions reveals a distinct spatial pattern as illustrated in Figs 4 and 5: (a) A layer of high shear extending along the wall in the liquid side of the fluid. This layer is more pronounced in the advancing than the receding case; (b) A compression region extending along the vapor side of the interface. Furthermore, shear and compression are of the same order of magnitude, and exhibit a similar distribution, albeit with peaks located in different regions. In fact, in the receding case, the peak of energy dissipation in the vicinity of the contact line is slightly moved to the energetically more favorable vapor side.

The natural question then is whether shear and compression effects control contact line motion at the same rate. To address this, we successively lowered and raised the shear and bulk (or compressive) viscosities, η and ζ , respectively, as shown in Table II of Appendix F. As highlighted in the Appendix, contact line motion is more sensitive to changes of liquid than vapor shear viscosity. Interestingly, the opposite effect is seen for the bulk (or compressive viscosity) and now contact line motion is less sensitive to changes of liquid than vapor bulk viscosity. This is consistent with the locations of the high shear-layer and high compression regions, in the liquid and the vapor side of the contact line, respectively. The results also reveal that the bulk viscosity has a disproportionately high impact on the velocity of advancing contact lines at low temperatures.

Finally, like with the equilibrium case, the configuration for the liquid-vapour interface observed in Fig. 4 seems to persist for distances sufficiently far from the wall (the maximum value of y_2 depicted in the figure is 15 molecular diameters), and so it should enter the macroscale allowing us to connect the micro- with the macroscale for moving contact lines.

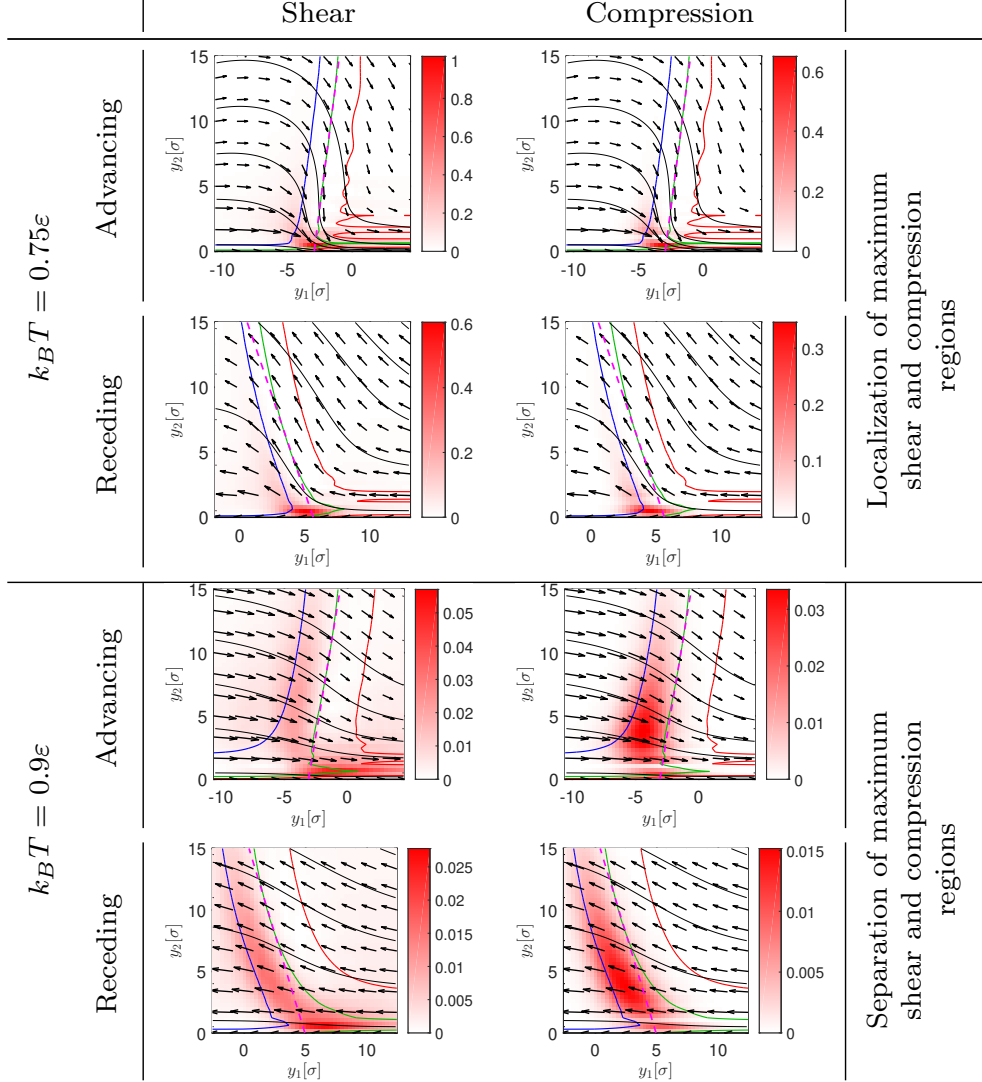


FIG. 4. When increasing the temperature, here from $k_B T = 0.75\varepsilon$ to 0.9ε , two regions emerge: a compressive region which favors the vapor side of the liquid-vapor interface, and a shear region in the vicinity of the wall. The plot represents the compressive and shear contributions to the viscous energy dissipation (see braces in Eq. 3) on a $15\sigma \times 15\sigma$ square domain next to the wall, normalized with U_{CL}^2 , in units of $1/\sigma^2$ for an advancing contact line (parameters as in Fig. 3). The blue, green and red isolines for the density represent values $(n - n_{\text{vap}}) / (n_{\text{liq}} - n_{\text{vap}}) = \{0.05, 0.5, 0.95\}$, respectively. For advancing contact lines, an effective slip region extends next to the wall into the liquid side (slip is discussed in Appendix G). At high temperatures, the peak of the compression distribution is moved away from the wall. Velocity fields and streamlines are given relative to the moving contact line. For receding contact lines, the peak of the distributions is shifted to the vapor side.

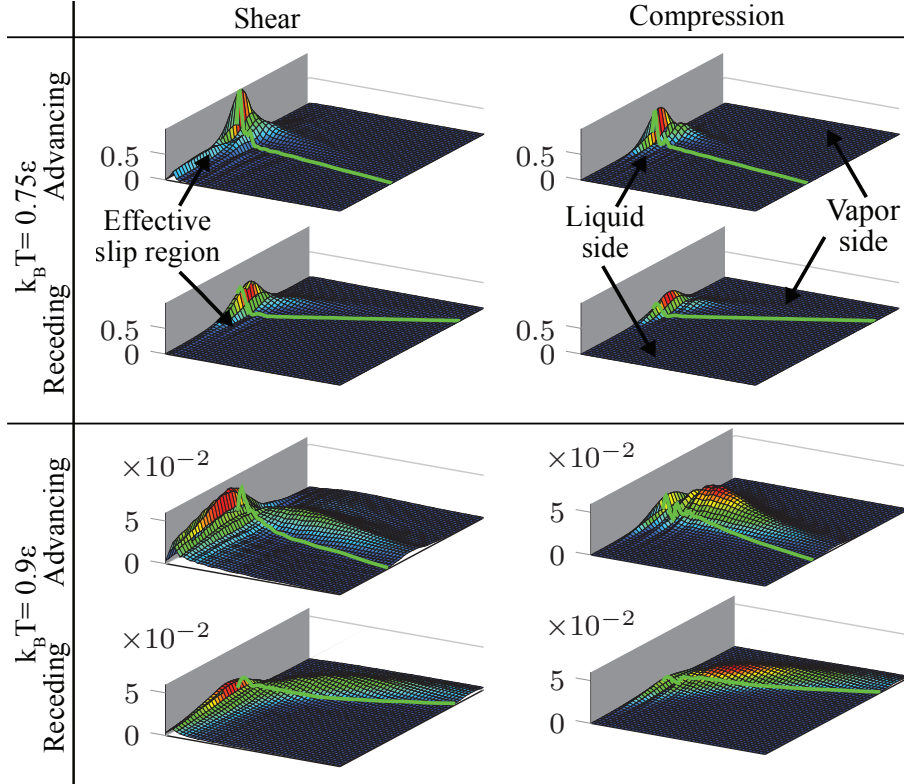


FIG. 5. Data as in Fig. 4, re-plotted here to emphasize magnitude of distribution in space.

V. EMERGENT CONTACT LINE BEHAVIOR AT THE MESOSCALE

Shear effects play an important role in controlling contact line motion in the vicinity of the contact line [45]. The thickness of the shear layer is of the order of a particle diameter and spreads along the wall into the liquid and vapor phases as the temperature is increased (see Fig. 4, and Figs. 12, 13 in Appendix E). It suggests the existence of an effective slip region interpolating between the no-slip region/wall and the bulk fluid. The width of this region is restricted by the oscillatory density structure induced by particle stratification close to the wall. Inferring the slip length from the velocity profile perpendicular to the wall reveals that, contrary to popular belief in fluid mechanics, it is not a robust parameter with respect to the choice of effective shear-layer thickness, precisely because of the fluid density oscillations in the vicinity of the wall (see Appendix G and Fig. 14 there). We thus infer that, whilst the first layer of fluid particles acts as a slip-facilitating layer, an effective slip length should be seen at best as an abstract coarse-grained parameter, of the order of the particle diameter, which includes more effects than just physical slip at an idealized

zero-thickness shear layer.

Conversely, the contact line friction coefficient μ_f turns out to be a more robust measure than the slip length as illustrated in Figs. 15–18) of Appendix H. It is precisely for this reason that it is used a benchmark for the accuracy of our numerical scheme in Appendix ???. It represents a relatively simple way to relate the contact angle θ with the contact line velocity U_{CL} :

$$\mu_f U_{CL} = \gamma_{lv} (\cos \theta - \cos \theta_{eq}), \quad (4)$$

and, like Young’s equation, it is valid all the way to the nanoscale even though it was obtained from macroscopic arguments.

The constitutive relation between the friction force per unit length and the off-equilibrium driving force can be constrained using MD simulations: Ren *et al.* [11] showed that nonlinear effects can indeed be neglected up to velocities of $\approx 1\sigma\tau^{-1}$, i.e. 50 times larger than the highest contact line velocities computed here. Figure 6 illustrates that Eq. 4 fits the (highly nonlinear and nonlocal) HDDFT well, both as the contact line equilibrates over time, and for varying initial conditions.

The contact line friction μ_f depends on temperature, the wall-liquid interaction strength, and shear viscosity. We now compare our results with an extension of the MKT model by Blake and De Coninck [46], based on activation energies of single particle displacements, to include viscous effects:

$$\mu_f = \left(\frac{v_L}{\bar{\lambda}^3}\right) \eta_{liq} \exp\left(\frac{\bar{\lambda}^2 \text{Wa}^0}{k_B T}\right), \quad (5)$$

where $\text{Wa}^0 = \gamma_{lv} (1 + \cos \theta_{eq})$ is the reversible work of adhesion, $\bar{\lambda}$ (also known as the Young-Dupré equation [47]) is the molecular displacement length, and v_L is the “volume of the unit of flow”. Here, the variations in the argument are small, and Eq. 5 can be linearized. Figure 7 reveals a very good agreement across temperatures and substrate strengths (the effect of changing the shear viscosity is illustrated in Fig. 19 of Appendix H). This linear relationship changes with the direction of flow: for both low and high temperatures, the contact line friction is approximately 50% lower for the receding compared to the advancing case, consistent with our computational result that dewetting is faster than wetting, as can be inferred from Fig. 6. The trends reported here also compare well with experimental data [48, 49], albeit with a different prefactor (see Fig. 7, right panel, Fig. 20 of Appendix H for a comparison with MD data). Unfortunately the range of data is not sufficient to infer straight

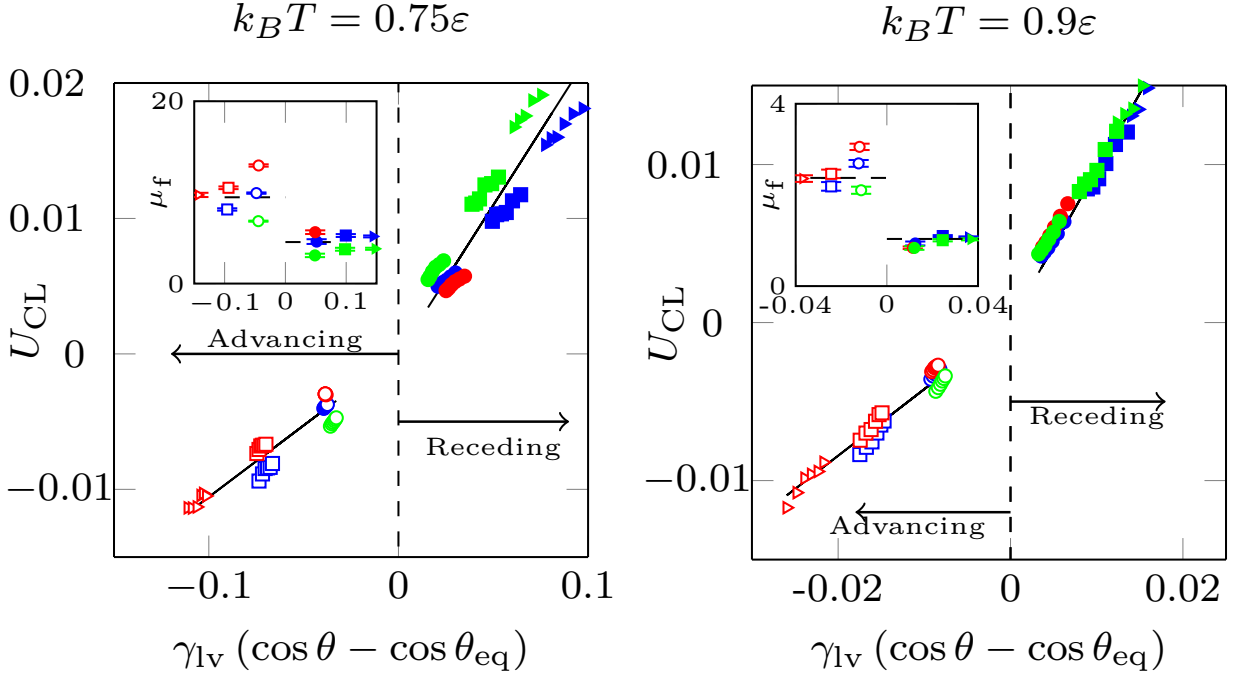


FIG. 6. Contact line velocity, U_{CL} , in multiples of $\sigma\tau^{-1}$ vs. force, $\gamma_{lv} (\cos \theta - \cos \theta_{eq})$, acting on the contact line in multiples of ϵ/σ^2 at times $t = 125 \dots 250\tau$ and $200 \dots 400\tau$. The black solid lines are fits to the prediction of Eq. 4 with resulting friction coefficients $\mu_f(k_B T = 0.75\epsilon) = (9.5, 4.5)$, $\mu_f(k_B T = 0.9\epsilon) = (2.4, 1.0)$ in multiples of $\sqrt{\epsilon m}/\sigma^2$ for the advancing and the receding case, respectively. Simulations with equilibrium contact angle θ_{eq} of 70° , 90° and 110° are represented by red, blue and green symbols, respectively. Circles, squares and triangles represent values with $|\theta_{eq} - \theta_{in}| = 10^\circ, 20^\circ$ and 30° , respectively. Filled and empty symbols represent receding and advancing contact lines, respectively. Insets display the contact line friction as a function of $\gamma_{lv}(\cos \theta_{in} - \cos \theta_{eq})$, in multiples of ϵ/σ^2 .

lines with full certainty. Let us also highlight that unlike MKT where the contact line friction is a free parameter, HDDFT enables to go a step further than MKT and benchmark the friction coefficient as a function of viscosity and the system's fundamental parameters, i.e. the strength of fluid-fluid and wall-fluid interactions, and temperature.

VI. CLOSING REMARKS AND DISCUSSION

We have coupled a particle-based approach, namely DDFT, with continuum hydrodynamics, to study an isothermal simple-fluid liquid-vapour contact line at low and high tem-

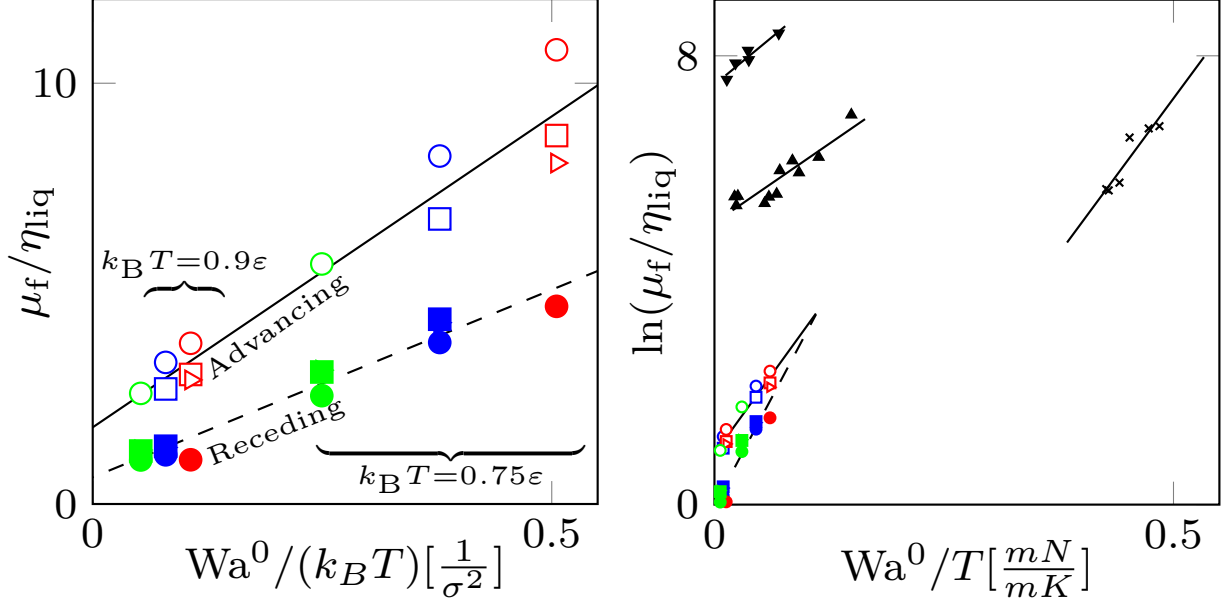


FIG. 7. Contact line friction μ_f varies with η_{liq} and $Wa^0/(k_B T)$. Left: Simulations towards equilibrium contact angles θ_{eq} of 70° , 90° and 110° are represented by red, blue and green symbols, respectively. Circles, squares and triangles represent values with $|\theta_{\text{eq}} - \theta_{\text{in}}| = 10^\circ, 20^\circ$ and 30° , respectively. Filled and empty symbols represent receding and advancing contact lines, respectively. Right: Black symbols are experimental data for spreading aqueous glycerol drops on glass (\times , [48]), a moving droplet of dodecane in water (\blacktriangle , [49]) and an air bubble in water (\blacktriangledown , [49]). For the data from [49], the sum of both fluid viscosities was used to rescale the contact line friction. Here, we have employed a typical value for the hard sphere diameter that of Argon, $\sigma = 3.3952\text{\AA}$, as a characteristic length scale for our data [50]. Black lines are linear fits to the data.

peratures. The resulting multiscale continuum framework, referred to as HDDFT, enables us to probe the nanoscale behavior of the moving contact line for a wide range of temperatures, including values relatively close to the critical point, a regime, which especially for liquid-vapour systems is notoriously difficult to capture. HDDFT avoids the limitations of other approaches, e.g. the small signal-to-noise ratios present in MD, but also experimental techniques, whilst still retaining information from the nanoscale through DFT.

Our computations with HDDFT suggest an intriguing length scale separation for large temperatures: energy dissipation due to shear effects is mostly concentrated at distances of a few particle diameters from the wall. Dissipation due to compressive effects, however,

exhibits a peak which extends into the vapour side of the fluid interface. Both shear and compression have a distinct impact on contact line motion which depends on direction and temperature. The width of the shear layer and associated effective slip region is controlled by the hard sphere particle diameter. In contrast, the compressive region is controlled by a temperature-dependent length scale. Interestingly, this compressive region is reminiscent of the interface layer stipulated by Shikhmurzaev in the context of the so-called interface formation model [15] – a detailed examination of the interface formation model was provided in our previous work in Ref. [51]. Its effect in fact is not negligible, as even in the limit of zero liquid shear viscosity, the contact line friction is approximately 50% of its original value (see Fig. 19 of Appendix H). This means that in addition to viscous effects in the bulk, slip effects at the wall, and dissipation in the thin-film regime, such as outlined by Ren *et al.* [11], the relative contribution of dissipation due to compressive effects needs to be taken into account and may offset contact line friction. We note, however, that in the spirit of the reductionist paradigm followed here, our model does not include a slip length and imposes instead the no-slip condition at the wall. This introduces a strong dissipative mechanism, in contrast to slip models or models of molecular displacement/MKT. Nevertheless, we can estimate that the dissipation-driven heat produced by the dynamics assuming isothermal conditions would lead to a temperature increase that would not exceed $k_B T/\varepsilon \approx 0.06$ (Appendix C). A schematic summarising the contact line regions and different approaches and models for contact line motion (slip, diffuse interfaces, interface formation model, MKT, MD and HDDFT in the present study), can be found in Fig. 8. The asymptotics of diffuse interface models for the moving contact line problem were analysed in detail in our previous works in Refs [37, 52].

Our study appears to corroborate experimental [48, 49, 56] and MD-based evidence [57] that the main source of dissipation stems from the deviation of the dynamic contact angle from its equilibrium value. HDDFT is also in line with the contact-line friction model (cf. Eqs. 4, 5), often referred to as (linear) MKT [10] – which starts from completely different model assumptions. This provides further evidence that the contact line friction, μ_f , acts as an abstract measure, similar to the slip length in the viscocapillary regime, reflecting the interplay of different physical effects at the nanoscale. However, extracting μ_f from the nanoscale is more robust than doing so for the slip length. In fact our computations show a generalised linear relationship between μ_f and $(\cos \theta - \cos \theta_{\text{eq}})$ across substrate strengths

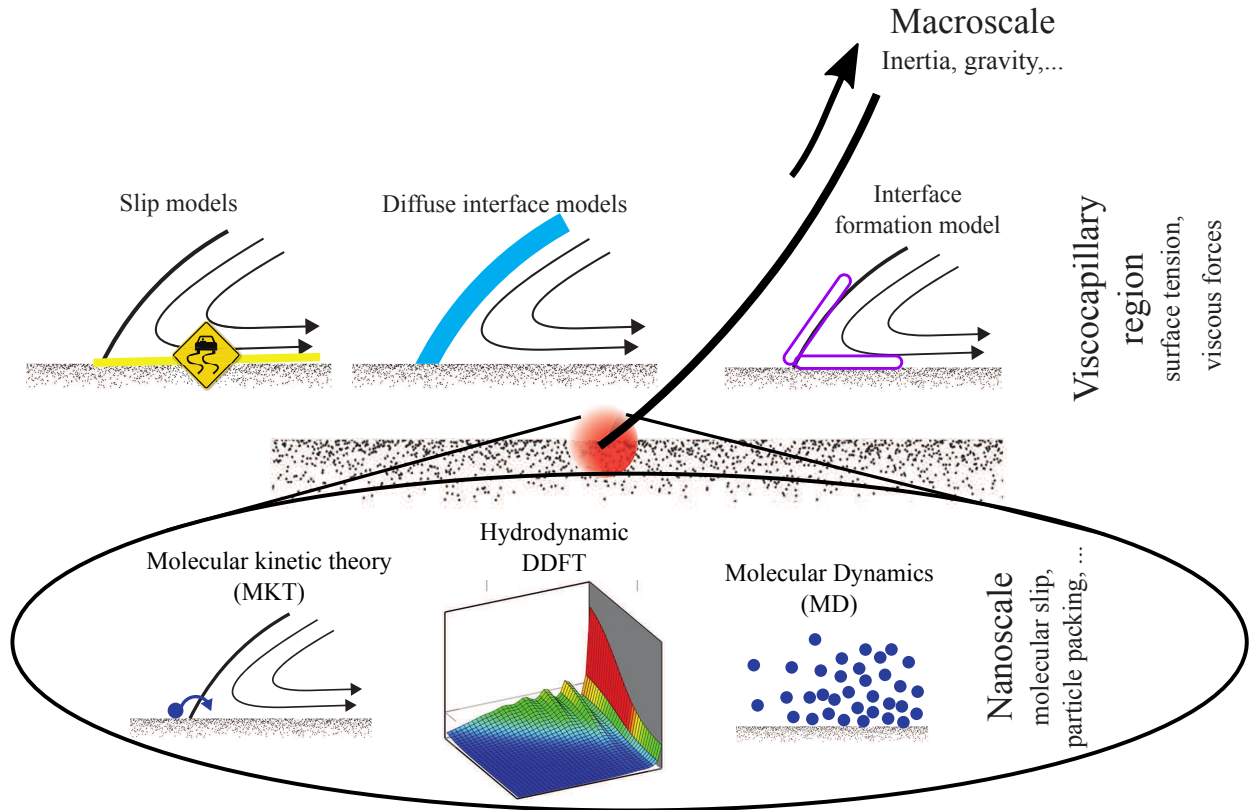


FIG. 8. Schematic of contact line regions and corresponding approaches and models. The viscocapillary region, discussed in the Introduction, is defined by a balance of surface tension and viscous forces. Slip models [53], diffuse interface models [36, 54, 55] and the interface formation model [15] resolve this regime. These models include at least one free parameter which captures the scale separation between the micro- and the macroscopic region. The behavior at the nanoscale is governed by various factors including microscopic slip, interfaces with finite thickness and surface layers in the region near to an interface between the liquid and the substrate-vapour. MKT [10, 46] resolves this region by postulating an activation energy for molecular displacement. MD resolves individual particles in space and time. The HDDFT model introduced in this work includes fluid layering and compressive and shear effects.

and temperatures as well as fluid viscosities, η_{liq} (Figs 6 and 19 of Appendix H). Quantitative comparison with experimental data [48, 49] reveals a similar rate of increase of $\log(\mu_f/\eta_{\text{liq}})$ with Wa^0/T in Eq. 5, where Wa^0 is the work of adhesion, across different fluid-substrate pairs, but with a different offset (Fig. 7, right panel). This difference may emerge from the influence of volatility in the compressible region at the liquid-vapor interface. Alternatively,

layering effects in the effective slip region close to the wall can affect contact line friction, such as observed close to complete wetting [58]. We note that no convex nanobending of the fluid interface as reported in the experiments by Chen *et al.* [59] is found here, but these authors considered (molecular) highly viscous non-volatile liquids.

ACKNOWLEDGEMENTS

We acknowledge financial support from Imperial College through a DTG International Studentship, the Joachim Herz foundation through an ‘‘Add-on Fellowships for Interdisciplinary Science’’, the ERC-EPSC Frontier Research Guarantee via Grant No. EP/X038645, the ERC via Advanced Grant No. 247031, and the EPSRC via Grant No. EP/L020564. We are grateful to the anonymous Referees for valuable comments and critical suggestions. Special thanks to Mr. Antonio Malpica-Morales from the Department of Chemical Engineering of Imperial for his assistance with Figs 10-13 and 15-18.

Appendix A: DFT

Equilibrium density distributions are computed employing classical DFT, which describes an equilibrium many-body system uniquely by a functional $\Omega[n]$ [60, 61], which is minimised with respect to the number density distribution n . For a single-component system,

$$\Omega[n] = \mathcal{F}[n] + \int n(\mathbf{r}) \{V_{\text{ext}}(\mathbf{r}) - \mu\} d\mathbf{r},$$

where at equilibrium \mathcal{F} is the intrinsic Helmholtz free-energy functional, V_{ext} is the external potential of the system and Ω is the grand potential. μ is the chemical potential, which tunes the system towards the liquid or the vapor state, here always chosen to be at equilibrium. We highlight that our DFT is formulated in a constant temperature – constant chemical potential ensemble.

The fluid is a simple LJ fluid with a potential with depth ε_{LJ} and length scale σ , and split $\mathcal{F}[n]$ into an ideal-gas contribution and contributions due to short-range hard-sphere exclusion effects, \mathcal{F}_{HS} , and long-range attractive interactions, $\mathcal{F}_{\text{attr}}$. \mathcal{F}_{HS} is approximated by Rosenfeld’s fundamental measure theory (FMT) [62, 63], with σ used as the hard-sphere diameter. Let us note here that FMT enables to capture the near-wall fluid layering leading to

oscillatory fluid density there, or indeed layering in the bulk fluid at freezing conditions/low temperatures, and, at equilibrium, it has been shown to be in excellent agreement with Monte Carlo simulations [42]. On the other hand, for liquid-vapour systems, the so-called local-density approximation (LDA) (e.g. [38, 64]) is sufficient as it captures the main features and is in qualitative agreement with more sophisticated approximations.

The attractive particle-particle interactions are treated in a perturbative mean-field manner [65–67] as

$$\mathcal{F}_{\text{attr}}[n] = \frac{1}{2} \iint \phi_{\text{attr}}(|\mathbf{r} - \mathbf{r}'|) n(\mathbf{r}) n(\mathbf{r}') d\mathbf{r}' d\mathbf{r},$$

where $\phi_{\text{attr}}(r) = 4\varepsilon_{\text{LJ}} ((\sigma/r)^{12} - (\sigma/r)^6) \Theta(r - \sigma)$ with radial cutoff at $r_c = 2.5\sigma$. The wall is also assumed to be LJ and V_{ext} is obtained by integrating the LJ wall-fluid particle interactions with depth ε_{wf} over a homogeneous flat wall. The wall then acts as a uniform effective boundary, thus sidestepping details about its atomistic makeup. For simplicity, the wall particles are assumed to have the same diameter as the fluid particles, σ . $\tau := \sigma \sqrt{\frac{m}{\varepsilon}}$ is the time scale, with m the particle mass. The energy scale is $\varepsilon := -\frac{9}{32\pi} \int_{\mathbb{R}^3} \phi_{\text{attr}}(|\mathbf{r}|) d\mathbf{r}$, which ensures that the bulk effect of the attractive contribution to the free energy $\int_{\mathbb{R}^3} \phi_{\text{attr}}(|\mathbf{r}|) d\mathbf{r}$ is independent of choice of the radial cutoff parameter r_c .

Appendix B: Colloidal and Molecular DDFT

Equations analogous to Eq. 2b but with damping term, have been derived in a statistical mechanics of fluids framework for colloidal fluids starting from the microscopic equations of motion of the individual particles [32, 33]. However, in contrast to colloidal fluids, for molecular or atomic fluids, no damping effect exists. The system is fully determined by Newton’s equations of motion at the molecular scale. Formally, this simplifies the equations and the link to the generalized momentum equation derived for colloidal systems can still be made by following the derivation of the continuity and momentum equations from Kramer’s equation as outlined in Refs. [32, 33, 68] and then setting the damping coefficient to zero. The main approximations that allow us to make progress are: (i) local equilibrium and expansion around local equilibrium; (ii) the adiabatic approximation, i.e. the higher-body correlations in the non-equilibrium fluid are approximated by those of an equilibrium fluid with the same density, and the corresponding sum rule holds out of equilibrium (statistical mechanical sum rules are discussed in [69]). The zeroth and first moment of Kramer’s

equation then yield:

$$\frac{\partial n}{\partial t} + \nabla \cdot (n\mathbf{u}) = 0, \quad (\text{B1a})$$

$$mn \left(\frac{\partial \mathbf{u}}{\partial t} + \mathbf{u} \cdot \nabla \mathbf{u} \right) = -n \nabla \left(\frac{\delta \mathcal{F}}{\delta n} \right) + \nabla \cdot \boldsymbol{\tau}, \quad (\text{B1b})$$

where $\boldsymbol{\tau} = \zeta (\nabla \cdot \mathbf{u}) + \eta ((\nabla \mathbf{u} + (\nabla \mathbf{u})^T) - \frac{2}{3}(\nabla \cdot \mathbf{u})\mathbf{I})$ is the stress tensor, \mathbf{u} is the fluid velocity, η is the usual shear or dynamic viscosity and ζ is the bulk viscosity accounting for compressible effects. Unfortunately, at this level of approximation the above system remains unclosed in that η and ζ depend on the first-order terms of the expansions of the one-body distribution and the two-body density, and cannot be written in closed form as functions of the local density or velocity. Here we follow [70] and employ empirical constitutive laws for the bulk and the shear viscosities as linear functions of density, interpolated between their liquid and vapour values, which for the shear viscosity can approximate MD well under certain conditions [8, 71]. Values for liquid and vapour viscosities correspond to MD results close to the saturation densities at temperatures T/T_{crit} ; see Table I.

$k_B T/\varepsilon$	$n_{\text{vap}}\sigma^3$	$n_{\text{liq}}\sigma^3$	γ_{lv}	η_{vap}	η_{liq}	ζ_{vap}	ζ_{liq}
0.75	0.028	0.622	0.285	0.10	1.2	0	5.5
0.9	0.086	0.458	0.072	0.15	0.8	0	2.0

TABLE I. Liquid and vapor shear and bulk viscosities for a simple fluid at different temperatures. Bulk densities and the surface tension are obtained from DFT computations. Critical temperature and densities from the DFT model are $k_B T_{\text{crit}}/\varepsilon = 1.001$ and $n_{\text{crit}}\sigma^3 = 0.246$. The liquid-vapor surface tension γ_{lv} is given in multiples of ε/σ^2 and viscosities are given as multiples of $\sqrt{\varepsilon m}/\sigma^2$. Shear viscosities are obtained from Figs. 7 and 8 of Ref. [72], and bulk viscosities from Fig. 4 of Ref. [73], both for the corresponding values of T/T_{crit} . It is noteworthy that the liquid viscosity data exhibits large variability with density, see e.g. also data in Ref. [74].

It is noteworthy that the HDDFT model we propose here represents an alternative approach to MD-based numerical methods [7, 9] to probe the link between basic nanoscale ingredients with the macroscale. But there are a few caveats and simplifying assumptions. Coupling of DFT in a hydrodynamic setting means that nonlocal correlations between the density profile and non-isotropic effects in momentum transport are not taken into account.

Instead, we assume scalars for the viscosities (local linear functional dependence of the viscosities on the density), and the stress tensor to be isotropic. Mean-field models also do not account for fluctuations [75, 76]. At temperatures close to the critical point, fluctuation-assisted nucleation, which we neglect here, may play a role for contact line movement [77]. We have extended the equations in B1b to include fluctuations [76]; this derivation is rigorous and supports the intuitive treatment of the original theory by Landau and Lifshitz of stochastic Navier-Stokes [78]. Accounting for these effects in contact line motion is not within the scope of the present study and needs to be tackled in future dedicated theoretical and computational work.

Appendix C: Analysis of temperature variation due to energy dissipation

The energy dissipated by shear and compression will heat up the fluid leading to local temperature changes. Here we assess these temperature changes. Analogous to Fig. 3, we employ molar heat capacity for gaseous [79] and liquid [80] Argon as a model system:

$$c_m = 18 \dots 21 \frac{J}{\text{mol} \cdot K} \approx 20 \frac{J}{\text{mol} \cdot K}. \quad (\text{C1})$$

For small perturbations, the local rate of temperature change can be approximated as:

$$\frac{k_B}{\varepsilon} \Delta \dot{T} = \frac{k_B}{\varepsilon} \frac{\dot{\varepsilon}_v}{c_m n} \quad (\text{C2})$$

$$\approx \frac{0.41}{\varepsilon} \frac{\dot{\varepsilon}_v}{n}. \quad (\text{C3})$$

Let us now compute an upper estimate for the temperature rise, by considering an advancing contact angle at $k_B T = 0.75\varepsilon$, which yields large levels of concentrated compression and shear in the vicinity of the contact line, as illustrated in Fig. 4. The contact line velocity for this case is approximately $U_{\text{CL}} = -0.01\sigma/\tau$ (see Fig. 10). Employing the larger values for liquid shear and bulk viscosities (see Table I) and the maxima of shear and compression shown in Fig. 4, we obtain that the viscous heat production in Eq. 3 and can be written as

$$\dot{\varepsilon}_v = U_{\text{CL}}^2 \left\{ \zeta \left(\frac{(\nabla \cdot \mathbf{u})^2}{U_{\text{CL}}^2} \right) + \eta \frac{\left((\nabla \mathbf{u} + (\nabla \mathbf{u})^T) - \frac{2}{3} (\nabla \cdot \mathbf{u}) \mathbf{I} \right)^2}{2U_{\text{CL}}^2} \right\} \quad (\text{C4})$$

$$\approx \left(0.01 \frac{\sigma}{\tau} \right)^2 \left\{ 1.2 \frac{\sqrt{\varepsilon m}}{\sigma^2} \cdot 1 \frac{1}{\sigma^2} + 5.5 \frac{\sqrt{\varepsilon m}}{\sigma^2} \cdot 0.6 \frac{1}{\sigma^2} \right\} \quad (\text{C5})$$

$$\approx 4.5 \cdot 10^{-4} \frac{\varepsilon}{\tau \sigma^3}, \quad (\text{C6})$$

where we used that $\tau = \sigma\sqrt{m/\varepsilon}$. Adopting an estimate for the density of $0.622\frac{1}{\sigma^3}$ (see Table I), leads after insertion into Eq. C3 to

$$\frac{k_B}{\varepsilon}\Delta\dot{T} \approx 3 \cdot 10^{-4}\frac{1}{\tau}. \quad (\text{C7})$$

Here we study quasi-steady contact line movement in a time window of between approximately 200τ and 400τ (see Fig. 10). Therefore, the total temperature change within this time window for the vicinity of the contact line does not exceed

$$\frac{k_B}{\varepsilon}\Delta T \approx 0.06, \quad (\text{C8})$$

leading to an increase from 0.75 to 0.81 for $k_B T/\varepsilon$. The true temperature increase is likely to be lower, as heat flux to areas neighboring the contact line and adjacent wall will likely reduce the localised heating effect.

Appendix D: Computational details

1. Numerical scheme

The density profiles are obtained using a highly accurate and robust pseudospectral scheme with 40 grid points in each direction, as described in our previous work in Ref. [42]. In short, the unit square $[-1, 1] \times [-1, 1]$ computational grid of Chebyshev polynomials is conformally mapped onto to the semi-infinite physical space, which aligns the grid with the initial contact angle. 50% of the discretization points are mapped onto $[-L_1, L_1]$ and $[0, L_2]$ in the y_1 and y_2 directions, respectively. For $k_B T = 0.75\varepsilon$, $L_1 = 4\sigma$ and $L_2 = 2\sigma$. For $k_B T = 0.9\varepsilon$, $L_1 = 6\sigma$ and $L_2 = 2\sigma$. The discretisation of the domain is skewed to increase the number of points near the fluid interface where higher gradients are expected. The convolution matrices needed for the FMT computations are also implemented using spectral methods. For this, different mappings of the collocation points from the computational to the physical domain are needed, depending on the proximity of the respective point from the wall (collocation points in the wall must be avoided).

To solve the dynamic equations, we employ the variable-step, variable-order solver `ode15s` from Matlab.

Independence of the results on the numerical grid and domain is shown in Fig. 9 using the contact line friction as a benchmark (contact line friction is discussed in detail in Sec. V

and detailed computations of this parameter are given in Figs. 15-18 of Appendix H). The initial configuration is a flat liquid-vapor interface at a contact angle θ_{in} to the wall

$$n_{\text{in}}(y_1, y_2; \theta_{\text{in}}) = n_{\text{wl}}(y_2)\hat{n}_{\text{lv}}(z) + n_{\text{wv}}(y_2)(1 - \hat{n}_{\text{lv}}(z)),$$

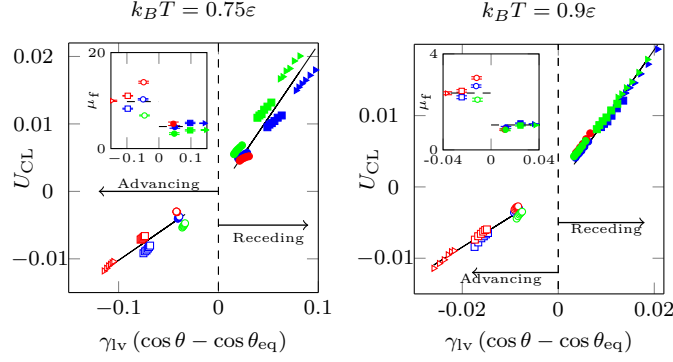
where $n_{\text{wl}}(y_2)$ and $n_{\text{wv}}(y_2)$ are the equilibrium density distributions of wall-liquid and wall-vapor interfaces, respectively, $\hat{n}_{\text{lv}} := (n_{\text{lv}}(z) - n_{\text{vap}}) / (n_{\text{liq}} - n_{\text{vap}})$ with $z := y_2 \cos \theta_{\text{in}} - y_1 \sin \theta_{\text{in}}$. As is evident from the figure, the scheme converges quickly with both the number of grids and computational domain.

2. Extracting contact angle, velocity and contact line friction

In Fig. 6, we plot the contact line velocity as a function of the force acting on the contact angle, effectively the difference between the contact angle and its equilibrium value, and extract pertinent information about the contact line friction. Monitoring the evolution of the contact line and contact angle in Figs. 10 and 11 of Appendix E ensures that the simulations are in a regime where any initial transients have died out and where temporal oscillations are reduced to an acceptable level. Typically, any transients fade away relatively quickly, at times of the order of a few of tens of τ at the most. Additionally, the near-wall density oscillations must be taken into account and an effective interface must be calculated as described in the caption of Fig. 10 of Appendix E.

The position of the contact line is determined by (dynamically) fitting the isoline for the density $(n - n_{\text{vap}}) / (n_{\text{liq}} - n_{\text{vap}}) = 0.5$ to the line $(y_{1,0} + \frac{y_2}{\tan \theta}, y_2)$ in an interval \mathcal{I} from the wall, with the contact line position $y_{1,0}$ and the inner region contact angle θ as fitting parameters. Once the contact line position, $y_{1,0}$, is determined, contact line velocity, U_{CL} , is defined as $U_{\text{CL}} := \frac{d}{dt}y_{1,0}$. In Figs. 15-18 of Appendix H we study the sensitivity of the contact angle and contact line velocity, U_{CL} , on the choice of the interval \mathcal{I} for the four cases depicted in Fig. 4.

An interval that is too close to the contact line is impacted by the highly oscillatory structure of the density profile there, and therefore leads to higher variability. In contrast, choosing an interval which is too wide, or too far away from the contact line, fails to capture the nanoscale dynamics. As discussed in Sec. V, plotting the contact line velocity U_{CL} versus the force acting on the contact line, $\gamma(\cos \theta - \cos \theta_{\text{eq}})$, reveals an approximately linear



Mean contact line friction $\mu_f [\sqrt{\varepsilon m}/\sigma^2]$	$k_B T = 0.75\varepsilon$		$k_B T = 0.9\varepsilon$	
	Adv	Rec	Adv	Rec
40 grid points per direction, $L_1 = 4\sigma, 6\sigma$ for $k_B T = 0.75\varepsilon$ and 0.9ε , respectively, $L_2 = 2\sigma$ (as in Fig. 6)	9.4653	4.5534	2.3737	1.0345
60 grid points per direction, $L_1 = 6\sigma, 8\sigma$ for $k_B T = 0.75\varepsilon$ and 0.9ε , respectively, $L_2 = 3\sigma$ (figures at the top)	9.7855	4.5888	2.3692	1.0390
80 grid points per direction, $L_1 = 8\sigma, 10\sigma$ for $k_B T = 0.75\varepsilon$ and 0.9ε , respectively, $L_2 = 4\sigma$	9.8246	4.6023	2.3675	1.0396

FIG. 9. Robustness of results to domain size and resolution. Top, figures: Parameters and symbols as in Fig. 6, but with a finer numerical grid with 60 points in each direction. The black solid lines are fits to the prediction of Eq. (4). Bottom, table: The friction coefficients μ_f obtained as fitting parameters of the black lines in the figure are compared with the results for lower resolutions, in multiples of $\sqrt{\varepsilon m}/\sigma^2$.

dependency. If not stated otherwise, we employed intervals $\mathcal{I} = [4.5\sigma, 7.5\sigma]$ and $[8.5\sigma, 11.5\sigma]$ for temperatures $k_B T = 0.75\varepsilon$ and 0.9ε , respectively.

3. Computational cost

The computations were done on a Windows Intel(R) Core(TM) i7-6700 CPU @3.40 GHz with 16.0GB RAM using MATLAB R2016a and take approximately 100 mins to compute

the convolution matrices for one contact angle setting, 20 mins for one equilibrium and 10-15 mins for one dynamic computation.

Appendix E: Dynamic evolution of receding and advancing contact lines and flow properties

Figures 10 and 11 provide a detailed overview of contact line behavior for different wetting and initial conditions for two different temperatures, $k_B T = 0.75\varepsilon$ and $k_B T = 0.9\varepsilon$, respectively.

Figures 12 and 13 display in detail a range of flow properties in the vicinity of the contact line for both advancing and receding contact lines.

Appendix F: Effect of changing viscosity on contact line motion

Here we explore the dependency of the contact line motion on shear and compressive effects shown in Figs 3 and 4. For this purpose we varied the shear and bulk viscosities, η and ζ , respectively. Changes in contact line speed, shown in Tab. II, inform us on the dependence of contact line motion on each effect. This leads to the following general observations:

1. Contact line motion is more sensitive to changes of liquid than vapor shear viscosity η . On the contrary, the sensitivity for bulk viscosity ζ is reversed, and contact line motion is more sensitive to changes in the vapor rather than in the liquid side. This result is consistent throughout all computations. It is in line with the location of the effective shear layer in the liquid side of the contact line and the peak of the compression in the vapor side of the contact line (see Fig. 5).
2. In general, advancing contact lines are more sensitive to changes in viscosity. This is especially pronounced for changes of the bulk viscosity in the low temperature regime ($k_B T = 0.75\varepsilon$).
3. In general, the low temperature regime is more sensitive to changes in viscosity compared to the high temperature regime. This is in line with the localization of the energy dissipation at the vicinity of the contact line for low temperatures. However,

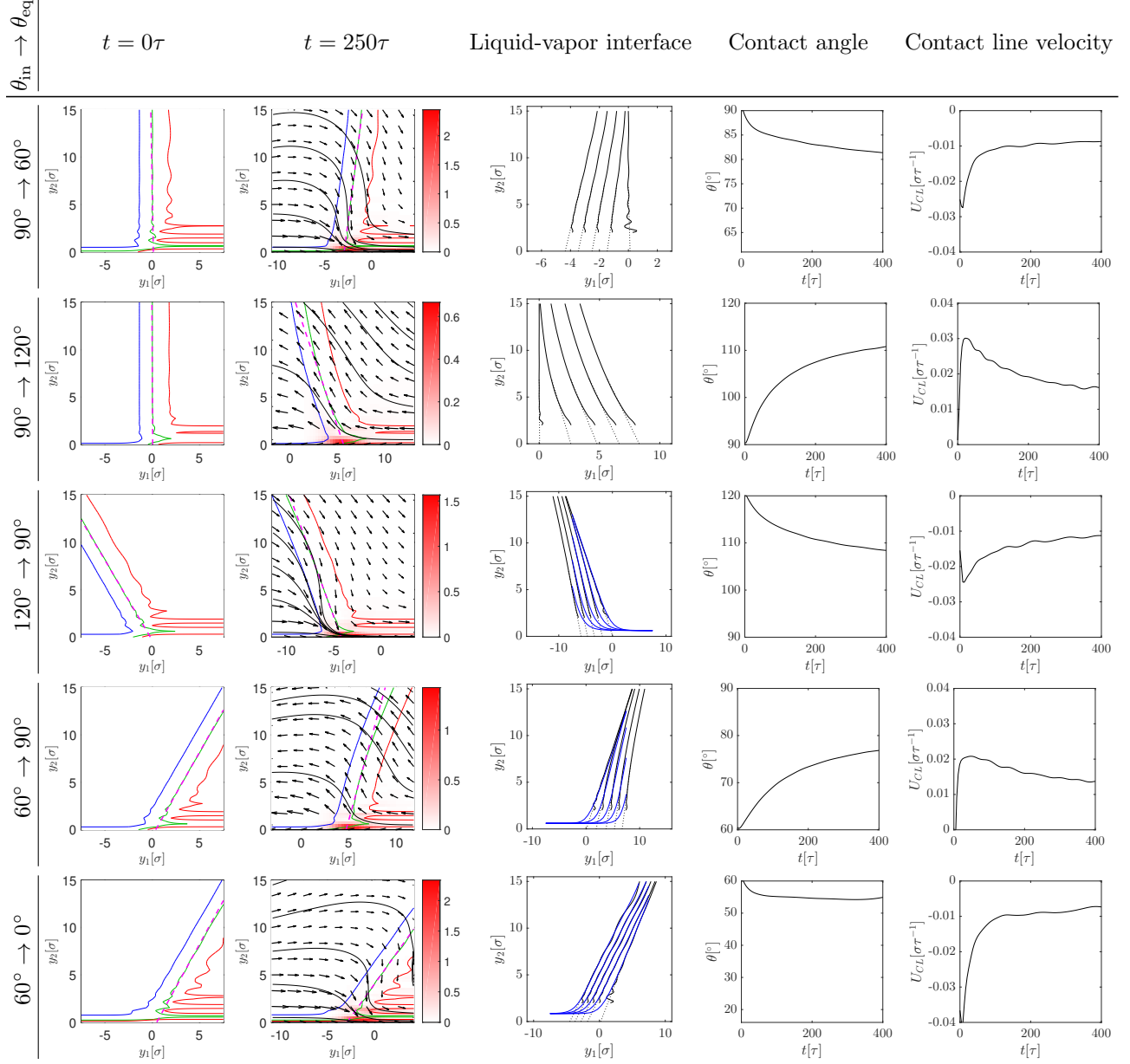


FIG. 10. Contact line behavior for different wetting and initial conditions for $k_B T = 0.75\epsilon$. Columns I and II: Density isolines, streamlines, and viscous energy dissipation at the moving contact line at the start of the simulation and at $t = 250\tau$. $y_{1,2}$ are the streamwise and cross-stream coordinates, respectively. Column III: Position of the liquid-vapor interface defined as the position where $n = (n_{\text{liq}} + n_{\text{vap}})/2$, at time points $t = 0, 100, 200, 300, 400\tau$ (black lines). Dotted lines are the linear interpolation of the liquid-vapor interface. For initial contact angles $\theta \neq 90^\circ$, the adsorption film thickness is represented by blue lines. Columns IV and V: Contact angle and contact line velocity over time, as obtained from the extrapolation of the dotted lines in column III. Velocities, velocity fields, and streamlines are given relative to the motion of the contact line.

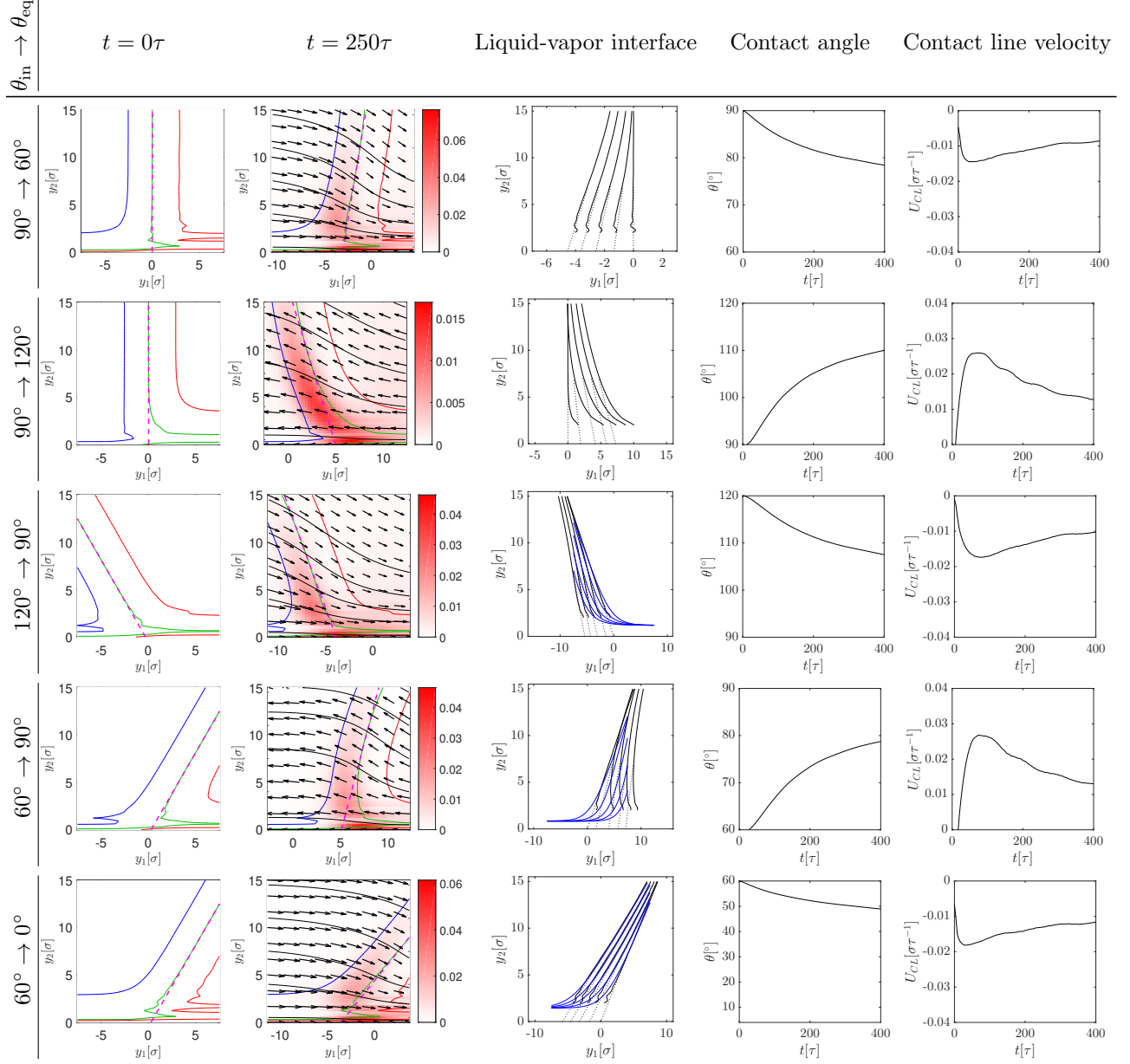


FIG. 11. Data as in Fig. 10, but for $k_B T = 0.9\epsilon$.

this trend is non-existent or reversed as far as the effect of compressive viscosity on receding contact lines is concerned.

- Changes in the liquid and vapor side can be superimposed to get the total change, i.e. increasing one viscosity first and then the other, is equivalent to increasing both at the same time.
- The sensitivity of contact line motion to increasing vs decreasing of the liquid side viscosities is the same.

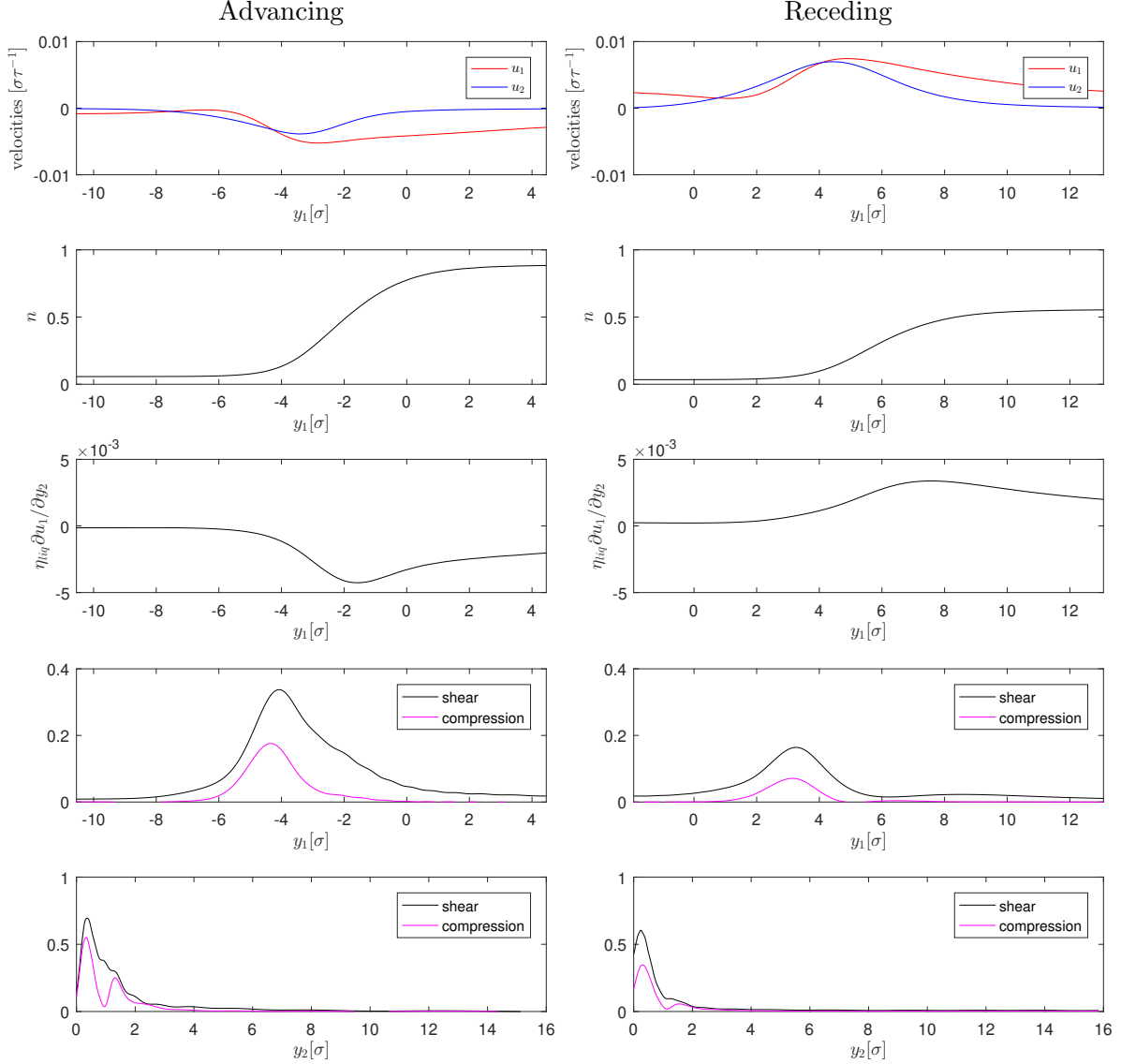


FIG. 12. Flow properties in the vicinity of the contact line for advancing and receding contact lines at $k_B T = 0.75\epsilon$ and at $t = 250\tau$, with parameters as in Fig. 4. The first four rows depict velocities $u_{1,2}$ in the $y_{1,2}$ directions, respectively, number density n , shear force, and shear and compressive effects parallel to the wall, at a distance of 1.1σ from the wall, corresponding to the bracketed quantities in Eq. 3. The bottom row depicts shear and compressive contributions parallel to the liquid-vapor interface, at a distance of 1σ into the vapor phase, again corresponding to the bracketed quantities in Eq. 3. The bottom two rows are analogous to Fig. 5.

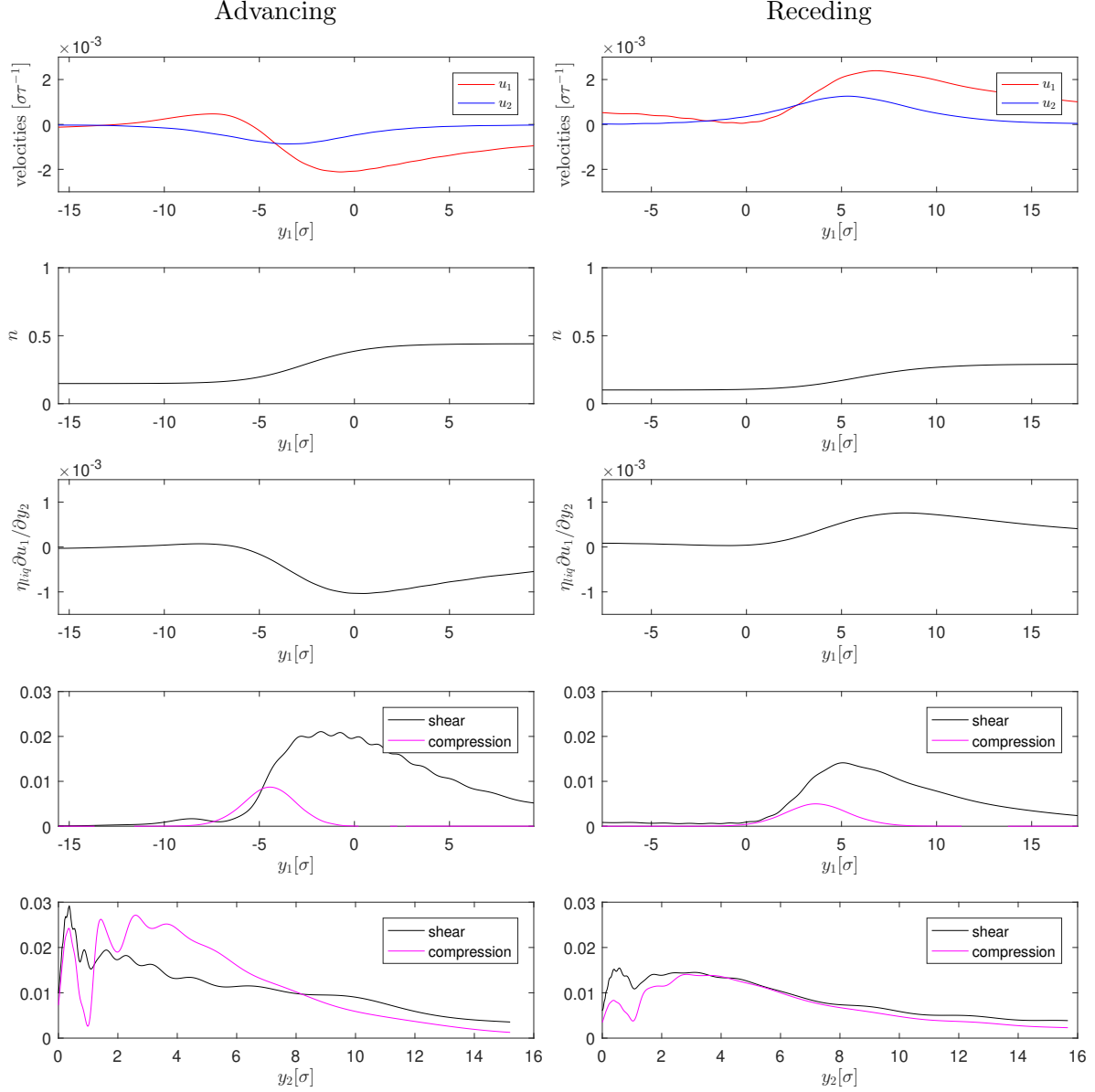


FIG. 13. Flow properties in the vicinity of the contact line for advancing and receding contact lines at $k_B T = 0.9\epsilon$ and at $t = 250\tau$, analogous to Fig. 12.

Appendix G: Extracting the slip length

The slip length establishes a linear relationship between the fluid velocity and shear at the wall. Given that in our DDFT computations we impose a no-slip condition at the wall, we can infer an effective slip length λ from the velocity profile at the liquid-vapor interface

$k_B T/\varepsilon$	Target CA	Δt , standard	Shear viscosity				Bulk viscosity				
			$\eta_{\text{liq}}, \eta_{\text{vap}} \uparrow$	$\eta_{\text{liq}} \uparrow$	$\eta_{\text{vap}} \uparrow$	$\eta_{\text{liq}} \downarrow$	$\zeta_{\text{liq}}, \zeta_{\text{vap}} \uparrow$	$\zeta_{\text{liq}} \uparrow$	$\zeta_{\text{vap}} \uparrow$	$\zeta_{\text{liq}} \downarrow$	
0.75	Adv	83°	207.1	28.5%	15.3%	11.5%	-14.1%	54.4%	21.3%	33.2%	-13.8%
0.75	Rec	97°	43.0	22.7%	13.5%	9.2%	-13.5%	14.4%	4.5%	10.6%	-5.0%
0.9	Adv	83°	159.2	18.5%	11.3%	6.7%	-11.4%	19.5%	5.7%	14.7%	-6.0%
0.9	Rec	97°	88.5	15.1%	8.9%	5.9%	-9.1%	16.8%	5.1%	12.5%	-5.5%

TABLE II. Changes in shear and compressive viscosity differentially affect contact line motion. Starting from initial contact angles $\theta_{\text{in}} = 90^\circ$, advancing (‘Adv’, $\theta_{\text{eq}} = 60^\circ$) and receding (‘Rec’, $\theta_{\text{eq}} = 120^\circ$) contact lines at two temperatures $k_B T = 0.75, 0.9\varepsilon$ are studied. The ‘standard’ configuration employs parameters as in Fig. 3. The fourth columns shows the time Δt in multiples of $\sigma\sqrt{m/\varepsilon}$ expired until the contact line reaches the target contact angle defined in the third column. The remainder of the table depicts relative changes of Δt with respect to the ‘standard’ configuration, if the bulk and shear viscosities are increased or decreased by 20% of the difference of the respective liquid and vapor viscosities.

and at a distance \bar{y}_2 to the wall:

$$\left. \frac{\partial u_1}{\partial y_2} \right|_{y_2=\bar{y}_2} (\lambda + \bar{y}_2) = u_1|_{\bar{y}_2}. \quad (\text{G1})$$

\bar{y}_2 may be interpreted as an effective shear layer thickness. Figure 14 shows velocities in a direction parallel to the wall and the slip lengths that may be extracted from those profiles as a function of \bar{y}_2 .

Physically, we expect that the slip length depends on the fluid density in the immediate vicinity of the contact line which is highly oscillatory in nature. Not surprisingly, the slip length is highly sensitive to the choice of the position \bar{y}_2 along the wall at which the velocity u_1 in Eq. G1 is taken, Indeed, in Fig. 14 it is shown that employing the velocity u_1 at three particle diameters away from the contact line into the vapor or liquid phase along the wall significantly affects the results for the slip length.

Similar challenges arise for MD or experimental slip measurements [6]. So, whilst the initial layer of fluid particles may well act as a slip-facilitating layer, the measurement of the slip length at the nanoscale and subsequent insertion into macroscopic models is problematic and does not lead to a robust prediction of macroscopic behavior. This means that whilst slip

models provide a convenient translational tool connecting different macro- and mesoscopic velocity and contact angle measurements [13], their interpretation of (effective) slip length is more attuned to that of an abstract coarse-grained parameter, as opposed to actual physical slip at the nanoscale (see also discussion in [81]).

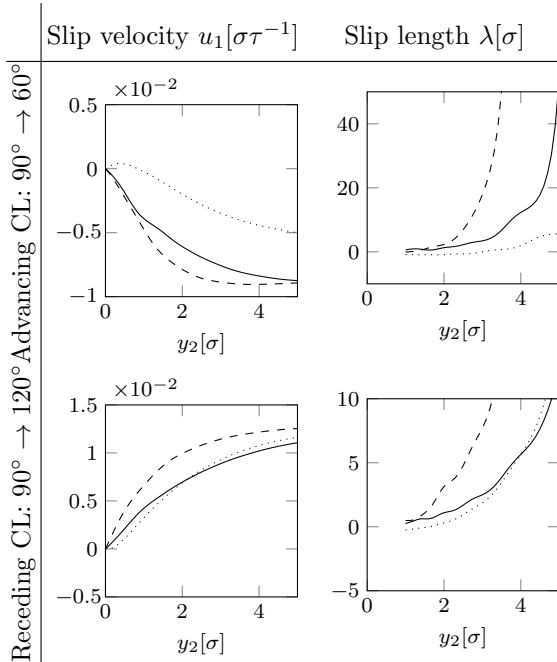


FIG. 14. Slip length computation for an advancing and receding contact line, with parameters as in the right plot of Fig. 3. Graphs in the left column depict the velocity u_1 in direction parallel to the wall as a function of the distance to the wall. The velocity is plotted along three trajectories perpendicular to the wall: crossing the contact line (solid lines), and shifted by 3σ towards the vapor and the liquid phase, depicted by dotted and dashed lines, respectively. The slip length is defined in Eq. G1 and is a function of the distance to the wall.

Appendix H: Contact line friction computations

Figures 15-18 present contact line friction computations illustrating the robustness of this parameter. Figure 19 illustrates the effect of shear viscosity on contact line friction and Fig. 20 reports a comparison with MD.

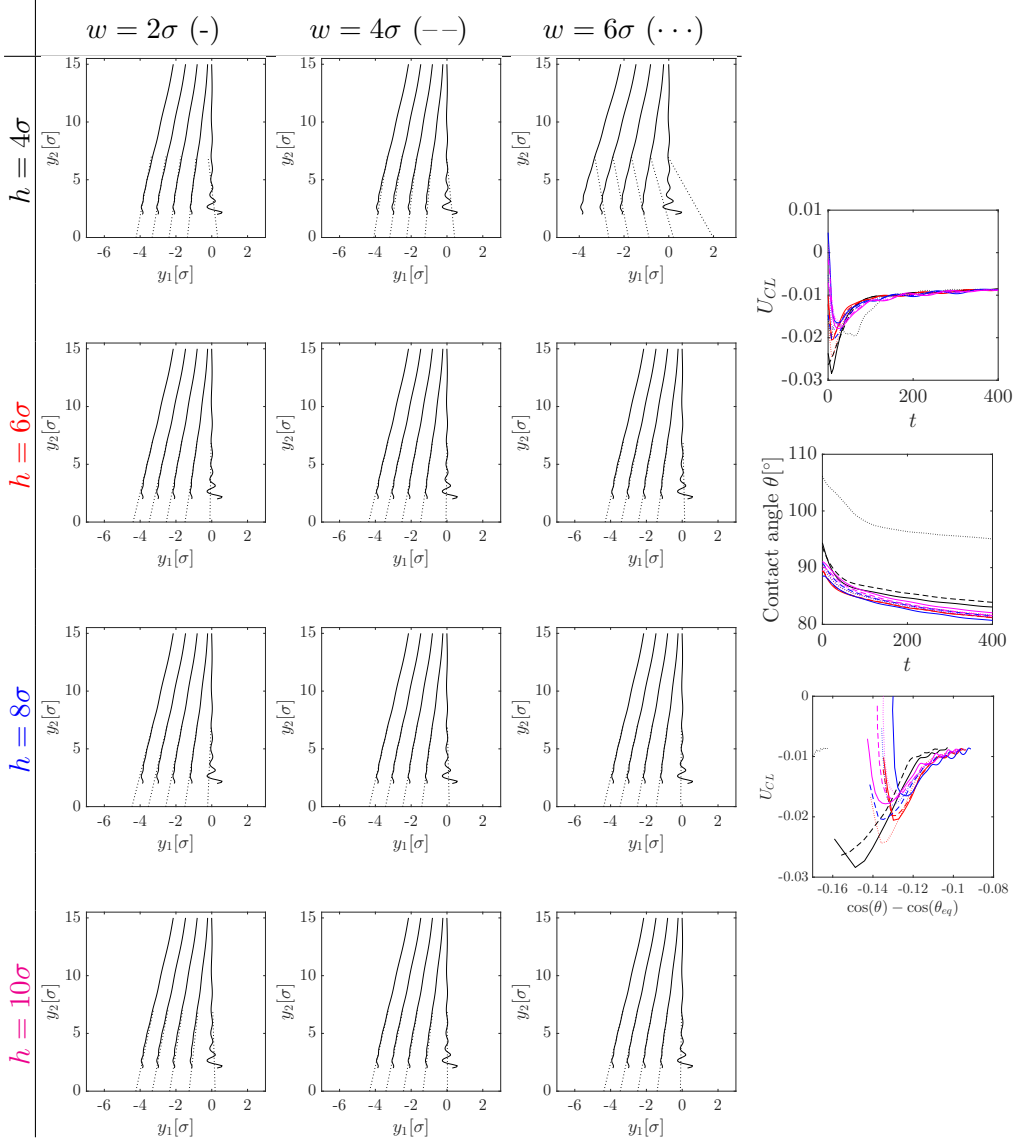


FIG. 15. Contact line friction for an advancing contact line, $90^\circ \rightarrow 60^\circ$ at $k_B T = 0.75\varepsilon$. Left panels: Linear interpolation (dotted lines) of the liquid-vapor interface (black lines). Different lines correspond to the interface at timepoints $t = 0, 100, 200, 300, 400\tau$. The dotted lines are obtained by interpolating the respective solid line in an interval of width w located at distance h from the wall, $\mathcal{I} = [h - w/2, h + w/2]$ (the size of interval \mathcal{I} was discussed in Appendix D). Right panels: Contact line velocity over time, contact angle over time, and crossplot of the two to extract the contact line friction. Black, red, blue, and magenta lines encode intervals at distance h equal to 4, 6, 8, and 10σ (corresponding to rows of the left panel). Solid, dashed, and dotted lines represent intervals of width $w = 2, 4, 6\sigma$ (corresponding to columns of the left panel).

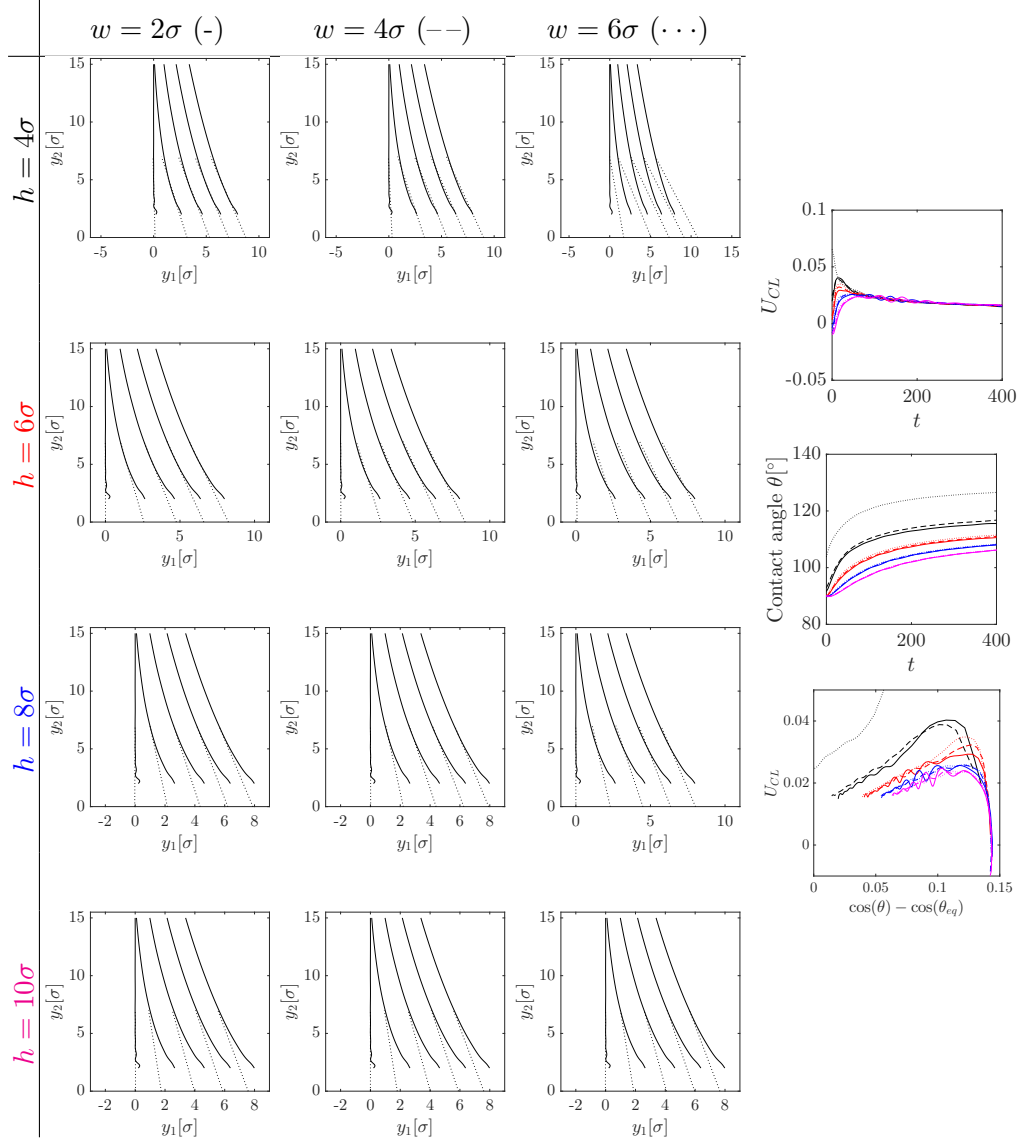


FIG. 16. Contact line friction for a receding contact line, $90^\circ \rightarrow 120^\circ$ at $k_B T = 0.75\varepsilon$. Details as in Fig. 15.

- [1] R. Lhermerout, H. Perrin, E. Rolley, B. Andreotti, and K. Davitt, A moving contact line as a rheometer for nanometric interfacial layers, *Nat Commun.* **7**, 12545 (2016); J.-S. Koh, E. Yang, G.-P. Jung, S.-P. Jung, J. H. Son, S.-I. Lee, P. G. Jablonski, R. J. Wood, H.-Y. Kim, and K.-J. Cho, Jumping on water: Surface tension-dominated jumping of water striders and robotic insects, *Science* **349**, 517 (2015).

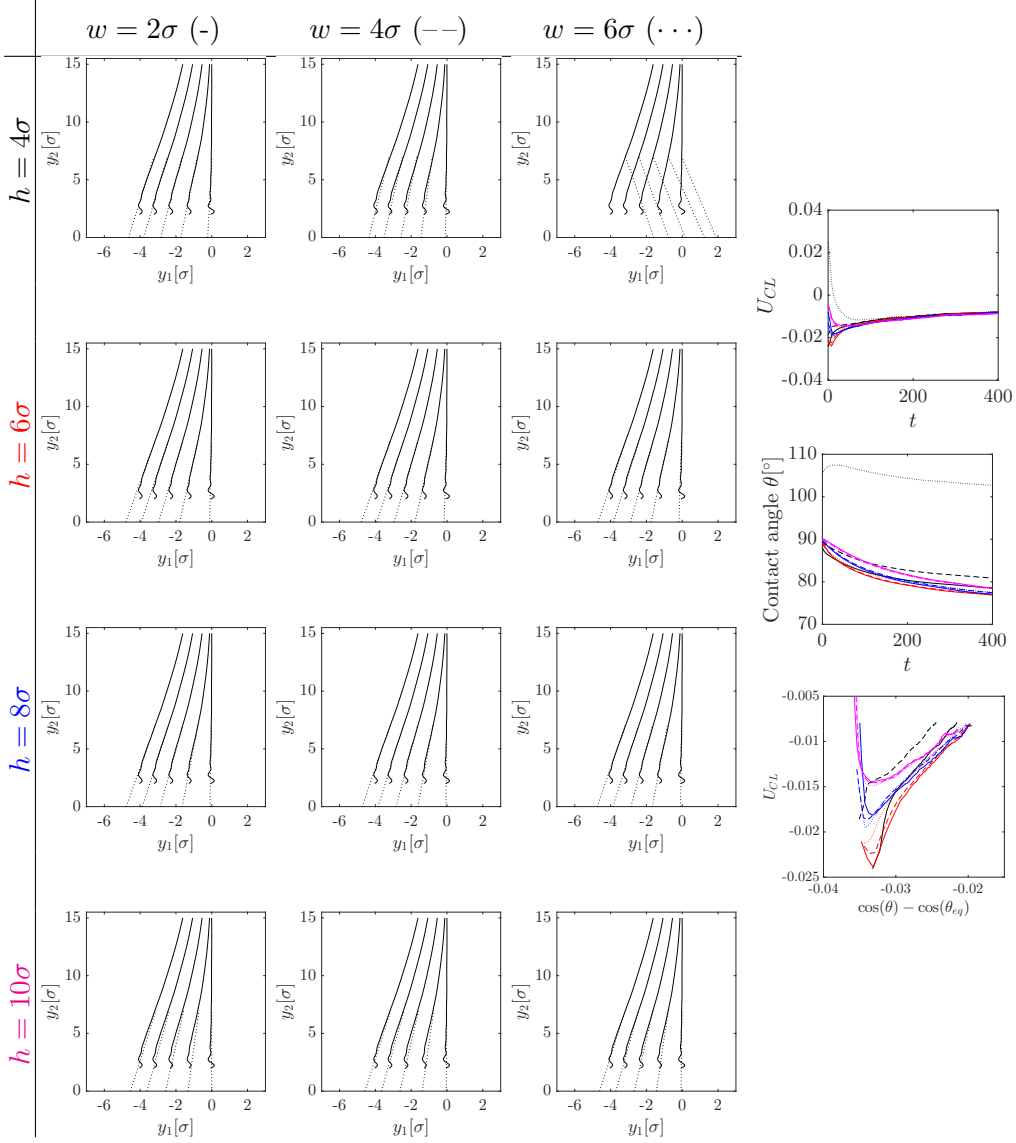


FIG. 17. Contact line friction for an advancing contact line, $90^\circ \rightarrow 60^\circ$ at $k_B T = 0.9\varepsilon$. Details as in Fig. 15.

- [2] C. Huh and L. E. Scriven, Hydrodynamic model of steady movement of a solid/liquid/fluid contact line, *J. Colloid Interface Sci.* **35**, 85 (1971).
- [3] D. Bonn, J. Eggers, J. Indekeu, J. Meunier, and E. Rolley, Wetting and spreading, *Rev. Mod. Phys.* **81**, 739 (2009).
- [4] E. Ramé, S. Garoff, and K. Willson, Characterizing the microscopic physics near moving contact lines using dynamic contact angle data, *Phys. Rev. E* **70**, 031608 (2004).
- [5] D. Seveno, A. Vaillant, R. Rioboo, H. Adao, J. Conti, and J. De Coninck, Dynamics of wetting revisited, *Langmuir* **25**, 13034 (2009).

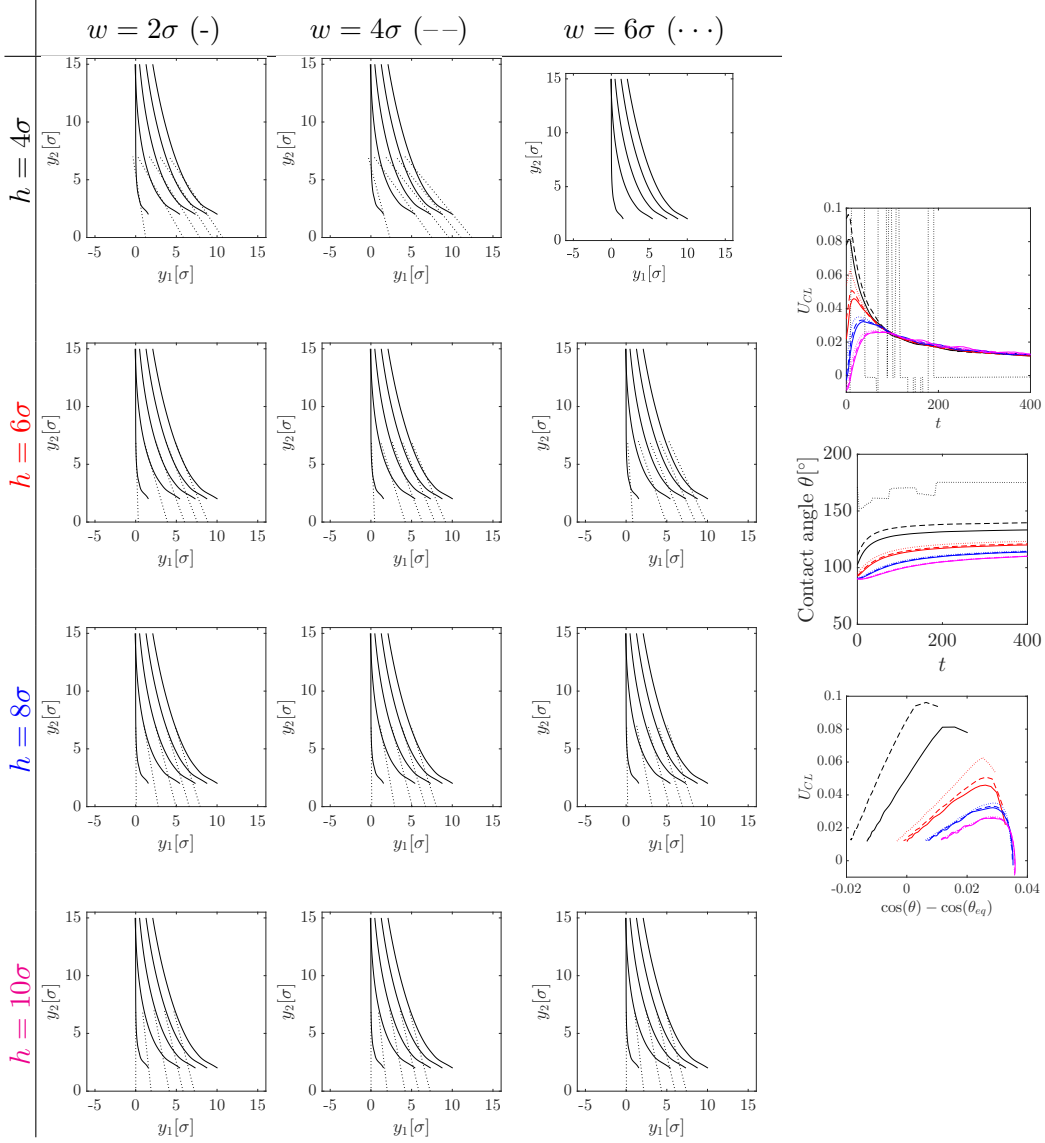


FIG. 18. Contact line friction for a receding contact line, $90^\circ \rightarrow 120^\circ$ at $k_B T = 0.9\epsilon$. Details as in Fig. 15. Note that for $h = 4\sigma$ and $w = 6\sigma$, the interface extends along the wall in the interval $\mathcal{I} = [1\sigma, 7\sigma]$, therefore not allowing for an effective fit.

- [6] J. Ralston, M. Popescu, and R. Sedev, Dynamics of wetting from an experimental point of view, *Annual Review of Materials Research*, Annu. Rev. Mater. Res. **38**, 23 (2008).
- [7] N. G. Hadjiconstantinou, Hybrid atomistic-continuum formulations and the moving contact-line problem, *J. Comput. Phys.* **154**, 245 (1999).
- [8] A. Russo, M. A. Durán-Olivencia, S. Kalliadasis, and R. Hartkamp, Macroscopic relations for microscopic properties at the interface between solid substrates and dense fluids, *J. Chem. Phys.* **150**, 214705 (2019).

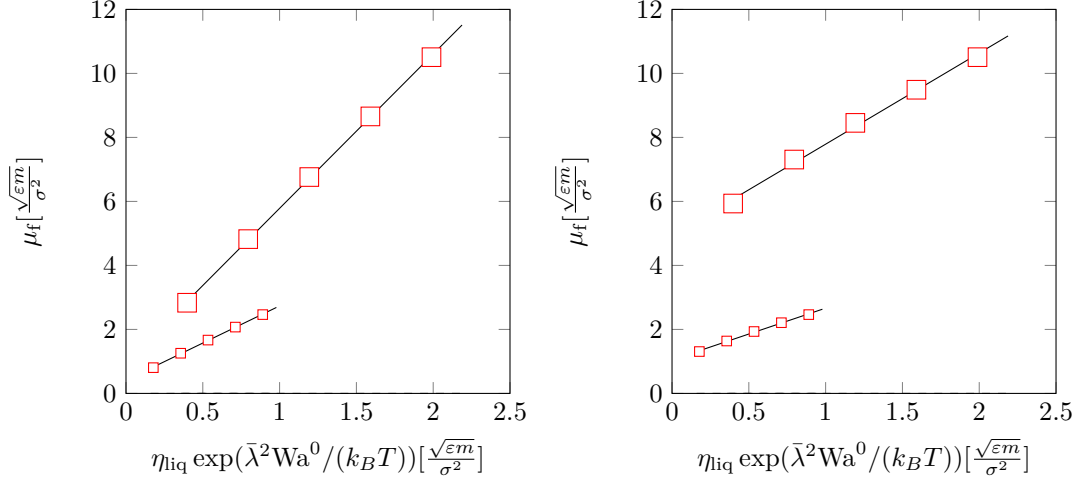


FIG. 19. Contact line friction measurements for varying viscosities, for an advancing contact line with $\theta_{\text{eq}} = 70^\circ$ and initial contact angle $\theta_{\text{in}} = 90^\circ$ for $k_B T = 0.75\epsilon$ and 0.9ϵ represented by large and small symbols, respectively. Left: All viscosities, i.e. bulk and shear viscosity for liquid and vapor phases, were scaled by $[0.2, 0.4, 0.6, 0.8, 1.0]$. Right: Only the liquid shear viscosity is scaled by $[0.2, 0.4, 0.6, 0.8, 1.0]$. Black lines are linear fits to the data. Scaling the liquid shear viscosity by 0.2 leads to a residual contact line friction of approximately 50% of its original value.

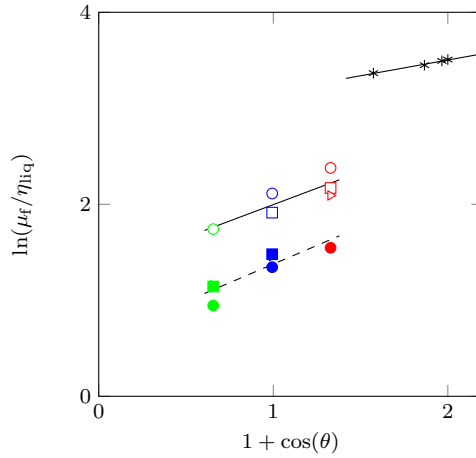


FIG. 20. Comparison of the contact line friction as in Fig. 7 for $k_B T = 0.75\epsilon$, with MD simulations Seveno and De Coninck [82] of capillary rise around a fiber of 16-atom-long liquid molecules, represented by $*$ -symbols. Black lines are linear fits to the data.

- [9] E. R. Smith, P. E. Theodorakis, R. V. Craster, and O. K. Matar, Moving contact lines: Linking molecular dynamics and continuum-scale modeling, *Langmuir* **34**, 12501 (2018).

- [10] T. D. Blake and J. M. Haynes, Kinetics of liquid/liquid displacement, *J. Colloid Interface Sci.* **30**, 421 (1969).
- [11] W. Ren, D. Hu, and W. E, Continuum models for the contact line problem, *Phys. Fluids* **22**, 102103 (2010).
- [12] P. Petrov and I. Petrov, A combined molecular-hydrodynamic approach to wetting kinetics, *Langmuir* **8**, 1762 (1992).
- [13] D. N. Sibley, A. Nold, and S. Kalliadasis, The asymptotics of the moving contact line: cracking an old nut, *J. Fluid Mech.* **764**, 445 (2015).
- [14] L. M. Hocking, The spreading of a thin drop by gravity and capillarity, *Q. J. Mech. Appl. Math.* **36**, 55 (1983); R. G. Cox, The dynamics of the spreading of liquids on a solid surface, Part 1. Viscous flow, *J. Fluid Mech.* **168**, 169 (1986).
- [15] Y. D. Shikhmurzaev, The moving contact line on a smooth solid surface, *Int. J. Multiph. Flow* **19**, 589 (1993).
- [16] T. Qian, X.-P. Wang, and P. Sheng, Molecular scale contact line hydrodynamics of immiscible flows, *Phys. Rev. E* **68**, 016306 (2003).
- [17] D. N. Sibley, A. Nold, N. Savva, and S. Kalliadasis, A comparison of slip, disjoining pressure, and interface formation models for contact line motion through asymptotic analysis of thin two-dimensional droplet spreading, *J. Eng. Math.* **94**, 19 (2014).
- [18] M. G. Velarde, *Discussion and Debate: Wetting and Spreading Science - quo vadis?*, Vol. 197 (Springer, 2011).
- [19] J. H. Snoeijer and B. Andreotti, Moving contact lines: Scales, regimes, and dynamical transitions, *Annu. Rev. Fluid Mech.* **45**, 269 (2013).
- [20] R. Evans, The nature of the liquid-vapour interface and other topics in the statistical mechanics of non-uniform classical fluids, *Adv. Phys.* **28**, 143 (1979); J. Lutsko, Recent developments in classical density functional theory, *Adv. Chem. Phys.* **144**, 1 (2010).
- [21] J. Lutsko, How crystals form: A theory of nucleation pathways, *Sci. Adv.* **5**, eaav7399 (2019).
- [22] P. Yatsyshin, N. Savva, and S. Kalliadasis, Geometry-induced phase transition in fluids: Capillary prewetting, *Phys. Rev. E* **87**, 020402(R) (2013).
- [23] P. Yatsyshin, A. O. Parry, and S. Kalliadasis, Complete prewetting, *J. Phys.: Condens. Mat.* **28**, 275001 (2016).

- [24] O. Buller, W. Tewes, A. J. Archer, A. Heuer, U. Thiele, and S. V. Gurevich, Nudged elastic band calculation of the binding potential for liquids at interfaces, *J. Chem. Phys.* **147**, 024701 (2017).
- [25] P. Yatsyshin and S. Kalliadasis, Surface nanodrops and nanobubbles: a classical density functional study, *J. Fluid Mech.* **913**, A45 (2021).
- [26] P. V. Hai, A. Fortini, and M. Schmidt, Crustal structures in binary hard-sphere colloid-droplet mixtures with patchy cross interactions, *Phys. Rev. E* **101**, 012608 (2020).
- [27] A. J. Archer, M. C. Walters, U. Thiele, and E. Knobloch, Solidification in soft-core fluids: Disordered solids from fast solidification fronts, *Phys. Rev. E* **90**, 042404 (2014).
- [28] Y. Yu and W. J. J., Density functional theory for inhomogeneous mixtures of polymeric fluids, *J. Chem. Phys.* **117**, 2368 (2002).
- [29] D. Stopper, H. Hansen-Goos, R. Roth, and R. Evans, Remnants of the disappearing critical point in chain-forming patchy fluids, *J. Chem. Phys.* **152**, 111101 (2020).
- [30] S. Jain, A. Domik, and W. Chapman, Modified interfacial statistical associating fluid theory: A perturbation density functional theory for inhomogeneous complex fluids, *J. Chem. Phys.* **127**, 244904 (2007).
- [31] J. Wu, Density functional theory for chemical engineering: From capillarity to soft materials, *AIChE J.* **52**, 1169 (2006).
- [32] A. J. Archer, Dynamical density functional theory for molecular and colloidal fluids: A microscopic approach to fluid mechanics, *J. Chem. Phys.* **130**, 014509 (2009).
- [33] B. D. Goddard, A. Nold, N. Savva, P. Yatsyshin, and S. Kalliadasis, Unification of dynamic density functional theory for colloidal fluids to include inertia and hydrodynamic interactions: derivation and numerical experiments, *J. Phys.: Condens. Matter* **25**, 035101 (2013).
- [34] B. D. Goddard, R. D. Mills-Williams, M. Ottobre, and G. A. Pavliotis, Well-posedness and equilibrium behaviour of overdamped dynamic density functional theory, *arXiv* **2002.11663** (2020).
- [35] M. te Vrugt, H. Löwen, and R. Wittkowski, Classical dynamical density functional theory: from fundamentals to applications, *Adv. Phys.* **69**, 121 (2020).
- [36] D. N. Sibley, A. Nold, and S. Kalliadasis, Unifying binary fluid diffuse-interface models in the sharp-interface limit, *J. Fluid Mech.* **736**, 5 (2013).

- [37] D. N. Sibley, N. A., N. Savva, and S. Kalliadasis, The contact line behavior of solid-liquid-gas diffuse-interface models, *Phys. Fluids* **25**, 092111 (2013).
- [38] A. Pereira and S. Kalliadasis, Equilibrium gas-liquid-solid contact angle from density-functional theory, *J. Fluid Mech.* **692**, 53 (2012).
- [39] C. Wylock, M. Pradas, B. Haut, P. Colinet, and S. Kalliadasis, Disorder-induced hysteresis and nonlocality of contact line motion in chemically heterogeneous microchannels, *Phys. Fluids* **24**, 032108 (2012).
- [40] A. Nold, D. N. Sibley, B. D. Goddard, and S. Kalliadasis, Fluid structure in the immediate vicinity of an equilibrium three-phase contact line and assessment of disjoining pressure models using density functional theory, *Phys. Fluids* **26**, 072001 (2014).
- [41] A. Nold, D. N. Sibley, B. D. Goddard, and S. Kalliadasis, Nanoscale fluid structure of liquid-solid-vapour contact lines for a wide range of contact angles, *Math. Model. Nat. Phenom.* **10**, 111 (2015).
- [42] A. Nold, B. D. Goddard, P. Yatsyshin, N. Savva, and S. Kalliadasis, Pseudospectral methods for density functional theory in bounded and unbounded domains, *J. Comput. Phys.* **334**, 639 (2017).
- [43] A. Nold, L. G. MacDowell, D. N. Sibley, B. D. Goddard, and S. Kalliadasis, The vicinity of an equilibrium three-phase contact line using density-functional theory: density profiles normal to the interface, *Mol. Phys.* **116**, 2239 (2018).
- [44] G. Lebon, J. Casas-Vázquez, and D. Jou, *Understanding Non-equilibrium Thermodynamics: Foundations, Applications, Frontiers* (Springer-Verlag Berlin Heidelberg, Berlin, Heidelberg, 2008).
- [45] J. D. McGraw, T. S. Chan, S. Maurer, T. Salez, M. Benzaquen, E. Raphaël, M. Brinkmann, and K. Jacobs, Slip-mediated dewetting of polymer microdroplets, *Proc. Natl. Acad. Sci.* **113**, 1168 (2016), <http://www.pnas.org/content/113/5/1168.full.pdf>.
- [46] T. Blake and J. De Coninck, The influence of solid-liquid interactions on dynamic wetting, *Adv. Colloid Interface Sci.* **96**, 21 (2002).
- [47] M. Schrader, Young-Dupré revisited, *Langmuir* **11**, 3585 (1995).
- [48] D. Duvivier, D. Seveno, R. Rioboo, T. Blake, and J. De Coninck, Experimental evidence of the role of viscosity in the molecular kinetic theory of dynamic wetting, *Langmuir* **27**, 13015 (2011).

- [49] M. Ramiasa, J. Ralston, R. Fetzer, and R. Sedev, Contact line friction in liquid–liquid displacement on hydrophobic surfaces, *J. Phys. Chem. C* **115**, 24975 (2011).
- [50] J. Vrabec, J. Stoll, and H. Hasse, A set of molecular models for symmetric quadrupolar fluids, *J. Phys. Chem. B* **105**, 12126 (2001).
- [51] D. N. Sibley, N. Savva, and S. Kalliadasis, Slip or not slip? a methodical examination of the interface formation model using two-dimensional droplet spreading on a horizontal planar substrate as a prototype system, *Phys. Fluids* **24**, 082105 (2012).
- [52] D. N. Sibley, A. Nold, N. Savva, and S. Kalliadasis, On the moving contact line singularity: Asymptotics of a diffuse-interface model, *Eur. Phys. J. E* **36**, 26 (2013).
- [53] O. V. Voinov, Hydrodynamics of wetting, *Fluid Dynamics* **11**, 714 (1976).
- [54] P. Seppelcher, Moving contact lines in the Cahn-Hilliard theory, *Int. J. Eng. Sci.* **34**, 977 (1996).
- [55] D. M. Anderson, G. B. McFadden, and A. A. Wheeler, A phase-field model with convection: Sharp-interface asymptotics, *Physica D* **151**, 305 (2001).
- [56] L. Zhao and J. Cheng, Analyzing the molecular kinetics of water spreading on hydrophobic surfaces via molecular dynamics simulation, *Sci. Rep.* **7**, 10880 (2017).
- [57] A. V. Lukyanov and A. E. Likhtman, Dynamic contact angle at the nanoscale: a unified view, *ACS nano* **10**, 6045 (2016).
- [58] P. Wu, A. Nikolov, and D. Wasan, Capillary dynamics driven by molecular self-layering, *Adv. Colloid Interface Sci.* **243**, 114 (2017).
- [59] L. Chen, J. Yu, and H. Wang, Convex nanobending at a moving contact line: the missing mesoscopic link in dynamic wetting, *ACS Nano* **8**, 11493 (2014).
- [60] R. Evans, The nature of the liquid-vapour interface and other topics in the statistical mechanics of non-uniform, classical fluids, *Adv. Phys.* **28**, 143 (1979).
- [61] J. Wu, Density functional theory for chemical engineering: From capillarity to soft materials, *AIChE J.* **52**, 1169 (2006).
- [62] Y. Rosenfeld, Free-energy model for the inhomogeneous hard-sphere fluid mixture and density-functional theory of freezing, *Phys. Rev. Lett.* **63**, 980 (1989).
- [63] R. Roth, Fundamental measure theory for hard-sphere mixtures: a review, *J. Phys.: Condens. Matter* **22**, 063102 (2010).
- [64] P. Yatsyshin and S. Kalliadasis, Mean-field phenomenology of wetting in nanogrooves, *Mol. Phys.* **114**, 2688 (2016).

- [65] R. W. Zwanzig, High-temperature equation of state by a perturbation method. I. Nonpolar gases, *J. Chem. Phys.* **22**, 1420 (1954).
- [66] Y. Tang and J. Wu, A density-functional theory for bulk and inhomogeneous Lennard-Jones fluids from the energy route, *J. Chem. Phys.* **119**, 7388 (2003).
- [67] L. Böhling, A. A. Veldhorst, T. S. Ingebrigtsen, N. P. Bailey, J. S. Hansen, S. Toxvaerd, T. B. Schröder, and J. C. Dyre, Do the repulsive and attractive pair forces play separate roles for the physics of liquids?, *J. Phys.: Condens. Matter* **25**, 032101 (2013).
- [68] B. D. Goddard, A. Nold, N. Savva, G. A. Pavliotis, and S. Kalliadasis, General dynamical density functional theory for classical fluids, *Phys. Rev. Lett.* **109**, 120603 (2012).
- [69] J. R. Henderson, Statistical mechanical sum rules, in *Fundamentals of Inhomogeneous Fluids*, edited by D. Henderson (Dekker, New York, 1992) pp. 23–84.
- [70] D. N. Sibley, A. Nold, N. Savva, and S. Kalliadasis, The contact line behaviour of solid-liquid-gas diffuse-interface models, *Phys. Fluids* **26**, 092111 (2013).
- [71] M. Morciano, M. Fasano, A. Nold, C. C. Braga, P. Yatsyshin, D. N. Sibley, B. D. Goddard, E. Chiavazzo, P. Asinari, and S. Kalliadasis, Nonequilibrium molecular dynamics simulations of nanoconfined fluids at solid-liquid interfaces, *J. Chem. Phys.* **146**, 244507 (2017).
- [72] K. Meier, A. Laesecke, and S. Kabelac, Transport coefficients of the Lennard-Jones model fluid. I. Viscosity, *J. Chem. Phys.* **121**, 3671 (2004).
- [73] K. Meier, A. Laesecke, and S. Kabelac, Transport coefficients of the Lennard-Jones model fluid. III. Bulk viscosity, *J. Chem. Phys.* **122**, 014513 (2005).
- [74] V. G. Baidakov and S. P. Protsenko, Metastable Lennard-Jones fluids. III. Bulk viscosity, *J. Chem. Phys.* **141**, 114503 (2014).
- [75] L. G. MacDowell, J. Benet, N. A. Katcho, and J. M. G. Palanco, Disjoining pressure and the film-height-dependent surface tension of thin liquid films: New insight from capillary wave fluctuations, *Adv. Colloid Interface Sci.* **206**, 150 (2014).
- [76] M. A. Durán-Olivencia, P. Yatsyshin, B. D. Goddard, and S. Kalliadasis, General framework for fluctuating dynamic density functional theory, *New J. Phys.* **19**, 123022 (2017).
- [77] X. Xu and T. Qian, Contact line motion in confined liquid–gas systems: Slip versus phase transition, *J. Chem. Phys.* **133**, 204704 (2010).
- [78] L. D. Landau, E. Lifshitz, and L. P. Pitaevskii, *Statistical Physics* (Oxford: Pergamon Press, 1980).

- [79] M. Chase, J. Phys. Chem. Ref. Data Monogr., in *NIST-JANAF Thermochemical Tables* (Monograph, 1998) p. 1952.
- [80] C. Gladun, The specific heat of liquid argon, *Cryogenics* **11**, 205 (1971).
- [81] E. Benilov and M. Benilov, A thin drop sliding down an inclined plate, *J. Fluid Mech.* **773**, 75 (2015).
- [82] D. Seveno and J. De Coninck, Possibility of different time scales in the capillary rise around a fiber, *Langmuir* **20**, 737 (2004).